Computer Physics Communications 284 (2023) 108595

Contents lists available at ScienceDirect

Computer Physics Communications

journal homepage: www.elsevier.com/locate/cpc

BinPo: An open-source code to compute the band structure of two-dimensional electron systems ☆,☆☆

Emanuel A. Martínez *, Juan I. Beltrán Fínez, Flavio Y. Bruno

GFMC, Departamento de Física de Materiales, Universidad Complutense de Madrid, 28040 Madrid, Spain

ARTICLE INFO

Article history:
Received 29 January 2022
Received in revised form 31 October 2022
Accepted 9 November 2022
Available online 17 November 2022

Keywords:
Python
2DES
Band structure
Maximally localized Wannier functions
$SrTiO_3$
Schrödinger-Poisson scheme

ABSTRACT

We introduce *BinPo*, an open-source Python code to compute electronic properties of two-dimensional electron systems. A bulk tight binding Hamiltonian is constructed from relativistic density functional theory calculations represented in the basis of maximally localized Wannier functions. *BinPo* has a Schrödinger-Poisson solver, integrating an electric field-dependent relative permittivity to obtain self-consistently the confining electrostatic potential energy term in the derived tight binding slab system. The band structure, energy slices, and other properties, along with different projections and orientations can be computed. High resolution and publishable figures of the simulations can be generated. In *BinPo*, priority has been given to ease-of-use, efficiency, readability and modularity, therefore becoming suitable to produce reliable electronic structures simulations at low computational cost. Along with the code itself, we provide files from first-principles calculations for some materials, instructions of use, and detailed examples of its wide range of capabilities. The code was developed with a focus on the ABO_3 perovskite structure-based systems, such as $SrTiO_3$ and $KTaO_3$, because of their increasing impact in the materials community. Some features, such as the projection onto orbital states, are restricted to calculations using the relevant t_{2g} orbitals for this family of materials, yet it is possible to include more elements in the basis for the band structure determination of other systems. The use of a relativistic approach allows for the inspection of the role of spin-orbit coupling and the resulting Rashba effect on the systems. We detail the approaches used in the code, so that it can be further exploited and adapted to other problems, such as adding new materials and functionalities which can strength the initial code scopes.

Program summary

Program title: *BinPo*
CPC Library link to program files: https://doi.org/10.17632/zk4xy7vfy4.1
Developer's repository link: https://github.com/emanuelm33/BinPo
Code Ocean capsule: https://codeocean.com/capsule/0987578
Licensing provisions: GPLv3
Programming language: Python
External routines/libraries: NumPy, SciPy, Matplotlib, ASE.
Nature of problem: Compute the band structure and other electronic properties in two-dimensional electron systems.
Solution method: Construction of a slab Hamiltonian from one built using a basis of maximally localized Wannier functions. Solve the Schrödinger-Poisson scheme to get the self-consistent potential energy along the slab. Use this potential to compute the band structure and additional properties by solving the Schrödinger equation.
Additional comments including restrictions and unusual features: Other features included are the visualization of the self-consistent process and final solutions, band structure and energy slices with different projections. High resolution and customizable figures can be obtained in all cases.

☆ The review of this paper was arranged by Prof. Weigel Martin.

☆☆ This paper and its associated computer program are available via the Computer Physics Communications homepage on ScienceDirect (http://www.sciencedirect.com/science/journal/00104655).

* Corresponding author.
E-mail address: emanuelm@ucm.es (E.A. Martínez).

https://doi.org/10.1016/j.cpc.2022.108595

1. Introduction

In the year 2004 it was discovered that a high mobility two-dimensional electron system (2DES) is formed at the interface between the two insulating oxides $LaAlO_3$ (LAO) and $SrTiO_3$ (STO) [1]. This fascinating finding gave rise to an intense research effort in the oxide electronics community to better understand the underlying mechanisms, variations in physical properties and prospective applications of the 2DES. Later on, many different procedures for creating a 2DES were revealed, such as photon irradiation under high-vacuum of STO or electrolyte-gating the oxide surface, among others [2]. The fact that STO is easily doped by different methods makes difficult to elaborate a general theory explaining the origin of the 2DES in the vast amount of cases found [3]. Whereas in some cases purely electrostatic explanations are invoked, the presence of defects such as oxygen vacancies, appears of fundamental importance in others [4–7]. That is why it is remarkable that the electronic structure measured in different 2DES systems based on STO is almost indistinguishable [8–11]. Moreover, many other similarities are found in transport properties of different 2DES all based on STO crystals [12,13] and theoretical band structure calculations with different approaches [14–22].

Here we present a computational tool that allows for the calculation of the 2DES band structure in a variety of systems that is independent of the microscopic origin of the charge carriers. The reader interested in the theoretical details of this dependency is referred to [23]. The computational tool relies on the band bending potential that can be obtained by solving the Schrödinger-Poisson scheme [24]. This produces self-consistent (SC) solutions comprising a distribution of the charge and potential energy along the confinement direction, enabling the computation of many electronic properties. *BinPo*, which stands for tight **bin**ding-**Po**isson calculations, is an open-source Python code to compute 2DES band structure and other properties, where importance is given to ease-of-use and capability of reproducing direct measurements.

Calculations based on the same ideas were already presented in several publications in order to explain direct experimental measurements of the electronic structure of oxide based 2DES [8,10,25–27].

A few codes exist that perform similar tasks in conventional semiconductors: NextNano [28] which is widely used to simulate nanodevices with realistic geometries, 1D Poisson [29] employed for calculating energy band diagrams, and more recently, Aestimo1D [30], a program that allows simulating heterostructures in one dimension. All of them are Poisson-Schrödinger solvers allowing for the calculation of the SC potential energy and many other related properties in such semiconductor systems. To the best of our knowledge, none are yet available for studying oxide compounds with strong electric field dependence of the relative permittivity, as in the case of quantum paraelectrics, like STO and $KTaO_3$ (KTO), where the Poisson equation turns into non-linear. Our contribution here is to introduce a ready-to-use code that allows for the calculation of the band structure and more electronic properties in quantum confined 2DES. The already existing codes assume linear media for the Poisson equation, which is proper for semiconductors. In contrast, *BinPo* can also solve the non-linear Poisson equation with a plane-by-plane discretization. Moreover, *BinPo* can take any user-defined relative permittivity model as an input to solve the Schrödinger-Poisson scheme.

At the current stage, *BinPo* can compute systems with cubic or hexagonal crystal systems. The general features include: obtaining and visualizing SC solutions for the electronic density and confinement potential, band structure and energy slices calculations. The band structure is computed along a high symmetry path and can be projected onto a plane or set of planes. According to the system crystallography, different capabilities are available. In cubic systems *BinPo* allows to use the three main low-index directions for the quantum confinement ([001], [110] and [111]), while for hexagonal systems the confinement must be along the [001] direction. In the specific case of cubic systems with only the t_{2g} manifold, that is d_{xy}, d_{yz} and d_{xz} orbitals [31], there are several additional features in addition to the previous ones, such as: projection of the band structure, energy slices and electronic density onto the atomic orbitals and envelope wavefunctions calculations in the quantum-well. This is because some materials where the t_{2g} manifold is relevant, such as STO and KTO, are of topical interest for the oxide electronics community [32,33]. Notably, since the starting point is a relativistic density functional theory (DFT) calculation, *BinPo* allows for the study of the Rashba effect at oxide based 2DES [25,27,34] or at the so-called bulk Rashba semiconductors 2DES [35–37]. All the functionalities and the implementation in the *BinPo* code are explained and exemplified throughout the paper.

The manuscript is organized as follows: in Section 2 we describe the background and mathematical methods used, in Section 3 we describe the program and the main parameters, in Section 4 we show step by step examples of SC potential, band structure calculations and the other capabilities for the archetypal STO(001) 2DES. We compare some simulations to experimental results for the 2DES stabilized on STO(001) and for the bulk Rashba semiconductor BiTeBr. Finally, in Section 5 we summarize the work and present the conclusions.

2. Background and methods

The starting point to perform *BinPo* calculations is the Hamiltonian of a bulk system in the basis of maximally localized Wannier functions (MLWFs) [38,39]. Although several semi-empirical approaches exist to generate tight binding (TB) models, such as $k.p$ perturbation theory [40] and Slater-Koster method [41], it has been shown that the MLWFs act as an exact TB basis capturing all electronic features from first-principles calculations [39,42]. TB models from MLWFs basis, or simply MLWFs TB models, are widely used to obtain realistic results and accurately compute physical quantities [42]. In this section we will show the methodology used to solve the quantum-electrostatic problem in the system starting from the bulk Hamiltonian, and subsequently generating a slab Hamiltonian to add a potential energy term. Despite the generality used to describe the methodology, at this stage, *BinPo* is programmed to work with cubic and hexagonal crystal systems with arbitrary band manifolds. ABO_3 cubic perovskites using the t_{2g} manifold, have some extended post-processing features implemented because of their high impact in the oxide community, as mentioned in the introduction and exemplified in Section 4.

2.1. The tight binding Hamiltonian of bulk systems

The use of MLWFs basis enables to construct a set of Bloch-like states by performing a Fourier transform. Let $\mathbf{R}$ label the 3D real lattice vectors and α be the orbital index corresponding to a specific band. The transformation into k-space can be written as:

$$|\mathcal{W}_{\mathbf{k}\alpha}\rangle = \frac{1}{\sqrt{N}} \sum_{\mathbf{R}} e^{i\mathbf{k}\cdot\mathbf{R}} |\mathbf{R}\alpha\rangle \tag{1}$$

where the states $|\mathcal{W}_{\mathbf{k}\alpha}\rangle$ are the Bloch elements, $|\mathbf{R}\alpha\rangle$ are the elements of the MLWFs basis and N is the number of k-points in the first Brillouin zone. The orthonormalization of the MLWFs basis, $\langle \mathbf{R}'\alpha' \mid \mathbf{R}\alpha \rangle = \delta_{\mathbf{R}\mathbf{R}'}\delta_{\alpha\alpha'}$, next to the convention used in Eq. (1) implies that in the reciprocal space the orthogonality reads $\langle \mathcal{W}_{\mathbf{k}'\alpha'} \mid \mathcal{W}_{\mathbf{k}\alpha} \rangle = \delta_{\mathbf{k}\mathbf{k}'}\delta_{\alpha\alpha'}$. Typically, the states $|\mathcal{W}_{\mathbf{k}\alpha}\rangle$ are not eigenstates of the Hamiltonian, therefore the Hamiltonian matrix will be non-diagonal. The transfer integrals are found to be [39]:

$$H^{(\mathbf{k})}_{\alpha\alpha'} = \left\langle \mathcal{W}_{\mathbf{k}\alpha'} \mid \hat{\mathcal{H}}_{KS} \mid \mathcal{W}_{\mathbf{k}\alpha} \right\rangle = \sum_{\mathbf{R}} e^{i\mathbf{k}\cdot\mathbf{R}} H^{(\mathbf{R})}_{\alpha\alpha'} \tag{2}$$

where $\hat{\mathcal{H}}_{KS}$ is the Kohn-Sham (KS) Hamiltonian of first-principles calculations and $H^{(\mathbf{R})}_{\alpha\alpha'} = \langle \mathbf{0}\alpha' | \hat{\mathcal{H}}_{KS} | \mathbf{R}\alpha \rangle$ are the elements of the KS Hamiltonian projected onto the MLWFs basis. Note that the Schrödinger equation can be now solved quickly and straightforwardly by diagonalization to get the band structure of the bulk system.

The procedure to generate the MLWFs basis on top of first-principles calculations is known as Wannierization. To carry out this procedure we use the open-source Wannier90 code [43–45], which is a standard tool in the condensed matter community since it is interfaced within most of the commonly used first-principles programs, such as VASP, WIEN2k, Quantum Espresso, Abinit and SIESTA among others. While any of the programs mentioned produces the needed output files to generate the MLWFs basis, the examples in this paper were obtained from Quantum Espresso [46]. The details of these calculations for STO, as well as the details of the Wannierization, can be found in Appendix A.

The workflow to obtain the $H^{(\mathbf{R})}_{\alpha\alpha'}$ elements is the following: perform first-principles calculations, get the MLWFs basis by Wannierization selecting a specific manifold and then projecting the KS Hamiltonian onto this basis. In Wannier90 software the $H^{(\mathbf{R})}_{\alpha\alpha'}$ elements are saved to the *seedname_hr.dat* file and henceforth we refer to it as W90 file. We already provide several W90 files which are listed in Appendix A. The users could also add their own files following the stepwise instructions given in the *~/BPexamples* folder. The W90 file will be taken by *BinPo* to generate the slab Hamiltonian in k-space described in the next subsection.

2.2. The tight binding slab Hamiltonian

In order to extend the previous discussion of the bulk Hamiltonian to a specific slab model, we stablish a real space direction, normal to the desired slab face, with a unit vector $\hat{\mathbf{r}}_\perp$. Then, we separate the 3D real vectors into a longitudinal ($\mathbf{R}_\perp$) and transverse ($\mathbf{R}_\parallel$) contributions. So that $\mathbf{R} = \mathbf{R}_\parallel + \mathbf{R}_\perp$, with $\mathbf{R}_\perp = r_\perp \hat{\mathbf{r}}_\perp$, where $r_\perp$ is an integer index labeling the system plane and $\mathbf{R}_\parallel$ includes the lattice vectors perpendicular to $\hat{\mathbf{r}}_\perp$. In this way, in analogy to Eq. (2), the Fourier transform for a slab can be denoted as:

$$\begin{aligned} H^{(\mathbf{k}_\parallel)}_{\alpha\alpha' r_\perp r'_\perp} &= \left\langle \mathcal{W}_{\mathbf{k}_\parallel \alpha' r'_\perp} \mid \hat{\mathcal{H}}_{KS} \mid \mathcal{W}_{\mathbf{k}_\parallel \alpha r_\perp} \right\rangle \\ &= \sum_{\mathbf{R}_\parallel} e^{i\mathbf{k}_\parallel \cdot \mathbf{R}_\parallel} \left\langle \mathbf{0}\alpha' r'_\perp \mid \hat{\mathcal{H}}_{KS} \mid \mathbf{R}_\parallel \alpha r_\perp \right\rangle \end{aligned} \tag{3}$$

where now $|\mathbf{R}_\parallel \alpha r_\perp\rangle$ states are the elements of the MLWFs basis discretized by planes, which in turn have the associated $|\mathcal{W}_{\mathbf{k}_\parallel \alpha r_\perp}\rangle$ states in the k-space. The above formula is nothing other than the 2D Fourier transform at each plane applied on the projected KS Hamiltonian. The orthogonality relations in the real and reciprocal space are:

$$\begin{aligned} \left\langle \mathbf{R}'_\parallel \alpha' r'_\perp \mid \mathbf{R}_\parallel \alpha r_\perp \right\rangle &= \delta_{\mathbf{R}_\parallel \mathbf{R}'_\parallel} \delta_{\alpha\alpha'} \delta_{r_\perp r'_\perp} \\ \left\langle \mathcal{W}_{\mathbf{k}'_\parallel \alpha' r'_\perp} \mid \mathcal{W}_{\mathbf{k}_\parallel \alpha r_\perp} \right\rangle &= \delta_{\mathbf{k}_\parallel \mathbf{k}'_\parallel} \delta_{\alpha\alpha'} \delta_{r_\perp r'_\perp} \end{aligned} \tag{4}$$

Further comments on these slab orthogonalization relations can be found in Appendix D.

So far, the Hamiltonian matrix will be a block diagonal one with translation symmetry along the $\hat{\mathbf{r}}_\perp$ axis and it would range all over the space for $r_\perp \to \pm\infty$. Nevertheless, we are interested in the region of the space containing the crystal. In practice, the index $r_\perp$ must be truncated to model such a region. Let L be the number of planes in the slab, we state that the transfer integrals are strictly zero if any of $r_\perp, r'_\perp$ is outside of the $[0,\ L-1]$ range. The Hamiltonian matrix generated by this constraint, which we call the slab Hamiltonian matrix, is:

$$\mathrm{H}^{(\mathbf{k}_\parallel)} = \begin{pmatrix} H^{(\mathbf{k}_\parallel)}_{\alpha\alpha' 00} & H^{(\mathbf{k}_\parallel)}_{\alpha\alpha' 01} & H^{(\mathbf{k}_\parallel)}_{\alpha\alpha' 02} & & H^{(\mathbf{k}_\parallel)}_{\alpha\alpha' 0,L-1} \\ H^{(\mathbf{k}_\parallel)}_{\alpha\alpha' 10} & H^{(\mathbf{k}_\parallel)}_{\alpha\alpha' 11} & H^{(\mathbf{k}_\parallel)}_{\alpha\alpha' 12} & \cdots & H^{(\mathbf{k}_\parallel)}_{\alpha\alpha' 1,L-1} \\ H^{(\mathbf{k}_\parallel)}_{\alpha\alpha' 20} & H^{(\mathbf{k}_\parallel)}_{\alpha\alpha' 21} & H^{(\mathbf{k}_\parallel)}_{\alpha\alpha' 22} & & H^{(\mathbf{k}_\parallel)}_{\alpha\alpha' 2,L-1} \\ & \vdots & & \ddots & \vdots \\ H^{(\mathbf{k}_\parallel)}_{\alpha\alpha' L-1,0} & H^{(\mathbf{k}_\parallel)}_{\alpha\alpha' L-1,1} & H^{(\mathbf{k}_\parallel)}_{\alpha\alpha' L-1,2} & \cdots & H^{(\mathbf{k}_\parallel)}_{\alpha\alpha' L-1,L-1} \end{pmatrix} \tag{5}$$

where the main diagonal blocks $H^{(\mathbf{k}_\parallel)}_{\alpha\alpha' r_\perp r_\perp}$ correspond to the intraplane interactions, while the off-diagonal blocks $H^{(\mathbf{k}_\parallel)}_{\alpha\alpha' r_\perp r'_\perp}$ correspond to interplane ones. It should be noted that, according to Eq. (3), each block has a dimension equal to $N_\alpha \times N_\alpha$, with N_α the number of elements in the MLWFs basis. Therefore, the slab Hamiltonian matrix ($\mathrm{H}^{(\mathbf{k}_\parallel)}$) will have a dimension equal to $N_\alpha L \times N_\alpha L$ at each $\mathbf{k}_\parallel$-point. In Fig. 1 it can be seen a schematic diagram of the Hamiltonian matrix of Eq. (5). There, each block represents the $N_\alpha \times N_\alpha$ matrix of Eq. (3). The artificial color scale represents the maximum values of the transfer integrals square modules in the blocks, pointing out how the interactions vanish away from the main diagonal, namely, when considering interactions between planes that are further apart.

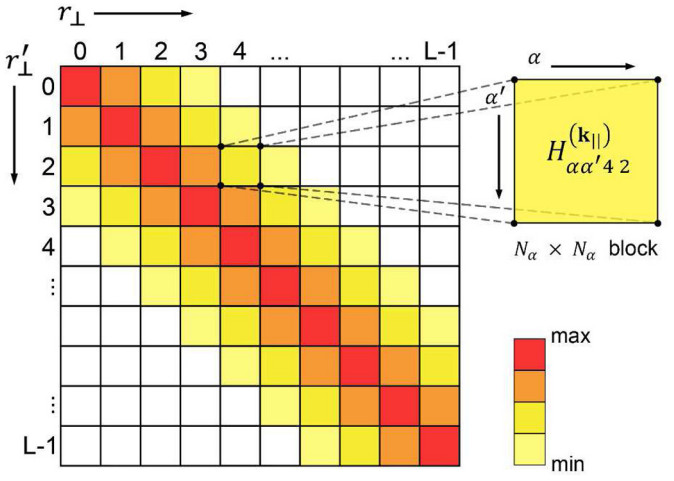

Fig. 1. Schematic diagram representing the Hamiltonian matrix of Eq. (5). Each block represents the $N_\alpha \times N_\alpha$ transfer integrals matrix of Eq. (3).

As mentioned in Section 2.1, α is the orbital index, which spans the manifolds involved in the problem (*i.e.* it spans the complete set of MLWFs). It reads:

$$\alpha = \left\{ 0^\uparrow, 0^\downarrow, 1^\uparrow, 1^\downarrow, \ldots, (N_\alpha/2-1)^\uparrow, (N_\alpha/2-1)^\downarrow \right\} \tag{6}$$

Where it should be noticed that the integer numbers represent the elements of the MLWFs basis with spins up ($\uparrow$) and down ($\downarrow$). In the particular case of the t_{2g} manifold it could be written as:

$$\alpha = \left\{ d^\uparrow_{yz}, d^\downarrow_{yz}, d^\uparrow_{zx}, d^\downarrow_{zx}, d^\uparrow_{xy}, d^\downarrow_{xy} \right\} \tag{7}$$

It is important to remark that the assignment of the MLWFs to atomic orbitals is not usually feasible. For the t_{2g} manifold, this is justified because there is almost no hybridization with other orbitals and the MLWFs are strongly localized and centered on the atomic nuclei, clearly exhibiting an atomic orbital character

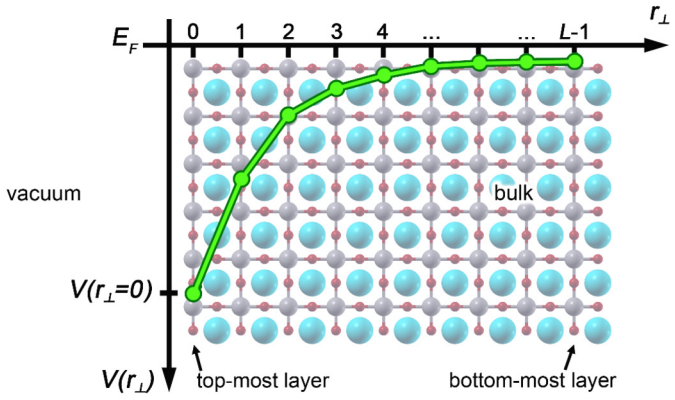

Fig. 2. Schematic picture of the system modeled by the slab Hamiltonian matrix with an additional on-site potential energy term.

[47]. These quantities are commonly quantified through the spread functional and the Wannier centers [39] (see Appendix A for some additional details). In the general case of Eq. (6) the assignment to any atomic orbital characters must be carefully analyzed and validated.

Since the goal is to obtain the electrostatic potential energy for the system, hereafter the SC potential, we take advantage of this expanded Hamiltonian matrix to add an on-site potential energy term. This potential energy is supposed to be homogeneous in the plane and should vary smoothly along $\hat{\mathbf{r}}_\perp$ axis. Later, this potential will lead to the possibility of obtaining a confined charge profile at the surface by solving the quantum-electrostatic problem in the slab. The slab Hamiltonian matrix with the potential term added reads:

$$\begin{pmatrix} H^{(\mathbf{k}_\parallel)}_{\alpha\alpha' 00} + \underline{V}(0) & H^{(\mathbf{k}_\parallel)}_{\alpha\alpha' 01} & \cdots & H^{(\mathbf{k}_\parallel)}_{\alpha\alpha' 0,L-1} \\ H^{(\mathbf{k}_\parallel)}_{\alpha\alpha' 10} & H^{(\mathbf{k}_\parallel)}_{\alpha\alpha' 11} + \underline{V}(1) & & H^{(\mathbf{k}_\parallel)}_{\alpha\alpha' 1,L-1} \\ \vdots & \vdots & \ddots & \vdots \\ H^{(\mathbf{k}_\parallel)}_{\alpha\alpha' L-1,0} & H^{(\mathbf{k}_\parallel)}_{\alpha\alpha' L-1,1} & \cdots & H^{(\mathbf{k}_\parallel)}_{\alpha\alpha' L-1,L-1} + \underline{V}(L-1) \end{pmatrix} \tag{8}$$

where the quantity $\underline{V}(r_\perp)$ represents the $N_\alpha \times N_\alpha$ potential energy matrix which affects each plane. We assume that this potential energy is applied on all the on-site elements in the same way, despite their orbital character and without promoting any electronic inter-orbital transition. In consequence, $\underline{V}(r_\perp) = V(r_\perp) \cdot \mathbb{1}_{N_\alpha \times N_\alpha}$, being $V(r_\perp)$ the potential energy per plane and $\mathbb{1}_{N_\alpha \times N_\alpha}$ the $N_\alpha \times N_\alpha$ identity matrix. A sketch of the system modeled by the matrix of Eq. (8) is depicted in Fig. 2.

Finally, we could write the TB slab Hamiltonian operator for this system in second quantization as:

$$\hat{\mathcal{H}}_{TB} = \sum_{\mathbf{k}_\parallel \alpha\alpha' r_\perp r'_\perp} \left(H^{(\mathbf{k}_\parallel)}_{\alpha\alpha' r_\perp r'_\perp} + \delta_{\alpha\alpha'}\delta_{r_\perp r'_\perp} V(r_\perp) \right) c^\dagger_{\mathbf{k}_\parallel \alpha r_\perp} c_{\mathbf{k}_\parallel \alpha' r'_\perp} \tag{9}$$

where $c^\dagger_{\mathbf{k}_\parallel \alpha r_\perp}$ and $c_{\mathbf{k}_\parallel \alpha' r'_\perp}$ are the creation and annihilation operators of one electron in the states $|\mathcal{W}_{\mathbf{k}_\parallel \alpha r_\perp}\rangle$ and $|\mathcal{W}_{\mathbf{k}_\parallel \alpha' r'_\perp}\rangle$, respectively.

2.3. The Schrödinger-Poisson scheme

To find out what is the SC potential energy of the system, the quantum-electrostatic problem using the well-known Schrödinger-Poisson scheme [24] must be solved. Our approach follows earlier work described in Refs. [48–50]. The main assumptions that we make are the following: (a) the crystal presents no defects and no structural relaxations, (b) electrons are uniformly distributed within a well-defined volume between adjacent planes, (c) after applying boundary conditions for the potential, the quantum-electrostatic problem is uniquely determined by the magnitude of the potential at the top-most layer, $V(0)$, and (d) the effect of polar distortions, without the need of establishing microscopic mechanisms, are taken into account within the relative permittivity model. This last assumption is based on some of the arguments given in Ref. [22]. Note that in the case of STO, the tetragonal distortions are not included [51] but their electric effects are captured by the permittivity model.

The Schrödinger-Poisson scheme solves self-consistently the potential energy $V(r_\perp)$ in the Schrödinger, charge density and Poisson equations. Then, a given convergence criterion is satisfied by obtaining, after a number of iterations, the output (V_{out}) sufficiently close to the input (V_{in}). Now, each of these four procedures are described.

2.3.1. The tight binding step

The time-independent Schrödinger equation for the slab TB Hamiltonian operator of Eq. (9) reads:

$$\hat{\mathcal{H}}_{TB}|\phi_{\mathbf{k}_\parallel n}\rangle = \epsilon_{\mathbf{k}_\parallel n}|\phi_{\mathbf{k}_\parallel n}\rangle \tag{10}$$

As in the bulk case, this equation is solved straightforwardly by diagonalizing the corresponding Hamiltonian matrix (Eq. (8)). Then, $N_\alpha L$ eigenenergies $\epsilon_{\mathbf{k}_\parallel n}$ are found at every $\mathbf{k}_\parallel$-point in reciprocal space. For each eigenenergy (enumerated by n index) there is an associated eigenstate, which is of dimension $N_\alpha L$. The obtained eigenstates can be expressed in terms of a set of complex coefficients $u^{\mathbf{k}_\parallel n}_{\alpha r_\perp}$ as:

$$|\phi_{\mathbf{k}_\parallel n}\rangle = \sum_{\alpha, r_\perp} u^{\mathbf{k}_\parallel n}_{\alpha r_\perp} |\mathcal{W}_{\mathbf{k}_\parallel r_\perp}\rangle \tag{11}$$

By applying the orthogonality relations of Eq. (4), coefficients $u^{\mathbf{k}_\parallel n}_{\alpha r_\perp}$ must satisfy the following normalization condition:

$$\sum_{\alpha, r_\perp} \left| u^{\mathbf{k}_\parallel n}_{\alpha r_\perp} \right|^2 = 1 \tag{12}$$

2.3.2. Charge density calculation

By means of the orthogonality relations given in Eq. (4), the charge density can be computed in term of the coefficients $u^{\mathbf{k}_\parallel n}_{\alpha r_\perp}$ as follows:

$$\rho(r_\perp) = -\frac{|e|}{\Omega_\perp N_\parallel} \sum_{\mathbf{k}_\parallel n} f\left(\epsilon_{\mathbf{k}_\parallel n}, T\right) \sum_\alpha \left| u^{\mathbf{k}_\parallel n}_{\alpha r_\perp} \right|^2 \tag{13}$$

where $|e|$ is the elementary charge, $N_\parallel$ is the total number of $\mathbf{k}_\parallel$-points used to discretize the first 2D Brillouin zone (BZ1), $f(\epsilon_{\mathbf{k}_\parallel n}, T)$ is the Fermi-Dirac function evaluated on the eigenenergy $\epsilon_{\mathbf{k}_\parallel n}$ at a temperature T, and $\Omega_\perp$ is the interplanar volume over which the electrons are uniformly distributed and it is defined as:

$$\Omega_\perp = \left\| \bar{a}_1 \times \bar{a}_2 \right\| \Delta r_\perp \tag{14}$$

where $\bar{a}_1$, $\bar{a}_2$ are the lattice vectors contained in $\mathbf{R}_\parallel$ and $\Delta r_\perp$ is the interplanar distance along the $\hat{\mathbf{r}}_\perp$ axis between two contiguous planes. Further details on the charge density formula and its validity are discussed in Appendix D.

2.3.3. The Poisson step

The Poisson equation as derived from the Gauss law is:

$$\frac{d^2 V(r_\perp)}{dr_\perp^2} = \frac{|e|}{\varepsilon_0 \varepsilon_r [E(r_\perp)]} \rho(r_\perp) \tag{15}$$

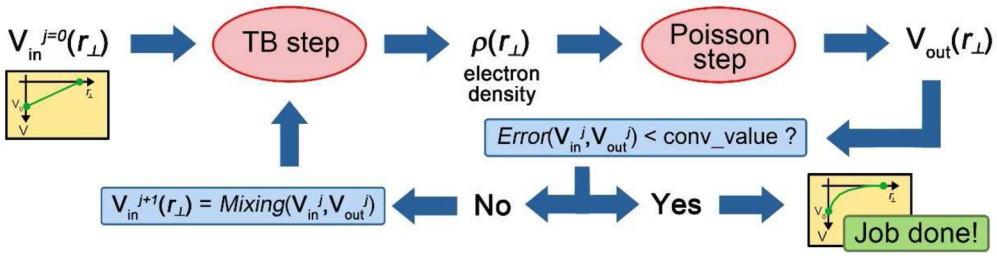

Fig. 3. Flowchart of the Schrödinger-Poisson scheme.

where ε_0 is the vacuum permittivity and ε_r is the relative permittivity. Typically, ε_r is constant for the vast majority of semiconductors and, in consequence, Eq. (15) would be linear. However, for other compounds ε_r can be a functional of the electric field, E. This introduces the non-linearity in the Poisson equation because E, in turn, depends on the potential energy as $E(r_\perp) = \frac{1}{|e|}\frac{dV}{dr_\perp}(r_\perp)$. In some cases, due to the quantum paraelectric nature of the involved materials [52–55] in the 2DES, ε_r strongly affects the potential energy profile along the slab.

In order to solve Eq. (15), which is a second order differential equation, it is necessary to specify two boundary conditions. In our approach, a Dirichlet boundary condition is used at the top-most layer, whereas either a Dirichlet or a Neumann one can be used at the bottom-most layer. The number of electrons in the 2DES is fixed by the boundary conditions and one must find the appropriate $V(r_\perp)$ that solves the Schrödinger-Poisson problem. Notice that the numbers of electrons can be found after solving the equations by integrating the charge density, but it is not a quantity that can be specified as an input parameter. In addition, the region deep inside the material for a thick enough system, close to the bottom-most layer, must have a zero electric field, *i.e.* $E(L-1) = 0$, and thus the potential is necessarily constant. These conditions can be formally met by taking a Neumann boundary condition, $dV/dr_\perp = 0$, and a sufficiently large number of planes. When running the code, sometimes it is convenient to use Dirichlet condition for a moderately lower number of planes, which will provide results quite accurate and a faster convergence. However, the potential obtained in this manner is not guaranteed to strictly represent the bulk $E(r_\perp)$, which should be zero for a sufficiently large $r_\perp$ as above mentioned, except in some very specific situations. A final check should be made in this case, comparing the potential obtained with Dirichlet conditions and a reduced number of planes with a calculation using Neumann condition at bottom-most layer and a large enough number of planes. A detailed comparison is shown in Appendix G where for the first 15 planes, the region where the 2DES lies in our example, the differences between the potential calculated for both boundary conditions are negligible. Other geometries and cases might require using different conditions to check that a correct physical situation is described by the calculation.

For a detailed derivation of Eq. (15), additional comments on boundary conditions, and the approach to get the relative permittivity models used here, we refer the reader to the Appendix E. *BinPo* also allows for including a small quantity of fixed background charge in Eq. (15). This approach is explained in Appendix C.

After solving the Poisson equation, we obtain an output potential energy (V^{out}) which can be compared with the input one to ensure electronic convergence, see Section 2.3.4. Further information on our approach to obtain and solve Eq. (15), as well as the implementation of boundary conditions, is provided in Appendix F.

2.3.4. Convergence criterion

The difference between the input and output potential energies obtained from the Poisson equation is calculated according to:

$$\chi^2 = \frac{1}{L}\sum_{r_\perp}\left(\frac{V^{out}(r_\perp) - V^{in}(r_\perp)}{V(r_\perp = 0)}\right)^2 \tag{16}$$

If this value is less than a defined convergence threshold at the j-th iteration, the SC solution is considered found. On the other hand, if this criterion is not satisfied, the over-relaxation mixing algorithm [48,56] generates a new input potential for the $(j+1)$-th iteration as:

$$V_{in}^{j+1}(r_\perp) = V_{in}^{j}(r_\perp) + f_{mix}\left(V_{out}^{j}(r_\perp) - V_{in}^{j}(r_\perp)\right) \tag{17}$$

with f_{mix} being the mixing factor. Generally, self-consistency is achieved for f_{mix} between 0.05-0.4 [48]. A flowchart of the whole Schrödinger-Poisson scheme is presented in Fig. 3.

Now, we will follow the scheme shown in Fig. 3 to summarize the algorithm. In the very first step (iteration $j = 0$) the initial potential energy and the boundary conditions are set. The initial potential is arbitrarily set to either a linear or exponential functional form. Insofar as we have tested, while both initial potentials produce the same SC solution, the exponential one could require less steps to reach the convergence for Neumann boundary condition at bulk. Then, a self-consistency loop is executed along the following steps at the j-th iteration:

(i) TB step: solve the Schrödinger equation for a potential energy V_{in}^{j}. This potential is properly added to the slab Hamiltonian matrix as indicated in Eq. (8), then the matrix is diagonalized to find the corresponding eigenvalues and eigenvectors.
(ii) Compute the electron density from the resulting eigenvalues and eigenvectors using Eq. (13).
(iii) Poisson step: solve the Poisson equation (Eq. (15)) to get a new potential energy V_{out}^{j}.
(iv) Convergence criterion: compare if V_{in}^{j} and V_{out}^{j} are equal up to a tolerance value according to the error value obtained in Eq. (16), else generate the input potential for the $(j+1)$-th iteration using Eq. (17) and return to point (i).

2.4. Post-processing steps

Once the quantum-electrostatic problem is solved, we have access to the electronic density and potential energy as a function of plane index satisfying some bulk value, inferred from DFT and boundary conditions, and certain value at the surface, typically motivated by experimental evidences. The $V(r_\perp)$ potential energy in the slab Hamiltonian operator of Eq. (9) is then replaced by the found SC potential. The eigenenergies and eigenstates coefficients obtained by solving this Schrödinger equation (Eq. (10)) provide important features of the system. This typically consists of specific quantities projected onto any of the system phase space dimensions (reciprocal k-points, orbitals of the manifold, plane sites,

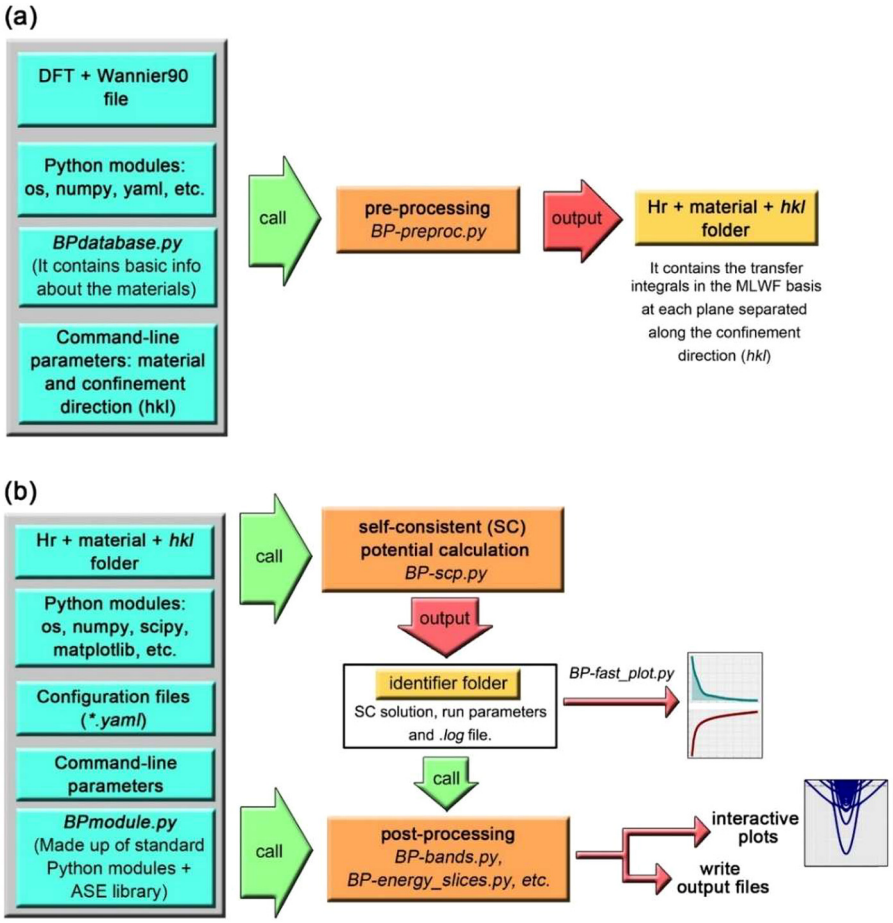

Fig. 4. Working structure of *BinPo*. (a) Pre-processing step. (b) Self-consistent potential energy calculation and post-processing steps.

etc.). For example, the band structure with different projections, the Fermi surface, or the electron density with orbital contributions among other quantities can be computed. This is referred to as the post-processing components which are enumerated and described in Appendix B. On the other hand, in Section 4 we will show how to execute each of the post-processing components through a set of examples.

3. Software description

BinPo was programmed in Python (version 3.x), which has become one of the most popular programming languages, especially for data science [57]. The libraries required to run the code are the standard ones NumPy [58], SciPy [59] and Matplotlib [60]. *BinPo* also uses the Atomic Simulation Environment (ASE) [61], which is a powerful Python library to perform atomistic simulations.

Firstly, *BinPo* requires to read a W90 file based on a relativistic first-principles calculation, whose main advantage is that all spin-orbit interactions are extracted from it. Therefore, spin-splitting and the associated phenomena, like avoided crossing [62–64] or Rashba effect [25,65,66], can be obtained as a direct consequence of the model. Despite that we already provide W90 input files for STO, KTO and BiTeBr with *BinPo*, the user could append other W90 files, for cubic or hexagonal crystallographic systems with different first-principles treatments and different band manifolds. This will take full advantage of the MLWFs TB model of the slab by capturing specific features from DFT calculations.

In the *BinPo* folder the user will find several Python files, which we name components. First of all, the user must execute the *BP-preproc.py* component for a pre-processing step. The working structure of this step can be seen in Fig. 4(a). This pre-processing consists of performing a separation of the matrix elements of the MLWFs TB Hamiltonian into planes along the $\hat{\mathbf{r}}_{\perp}$ axis. At present, this separation is performed up to eight planes (0 to 7), which results in energy differences between DFT and Wannierization bands below 10^{-3} eV, for the specific case of STO, and that we consider to be a good description of the system as we show in Fig. A.1 of the Appendix A. The *BP-preproc.py* component calls some standard Python modules and the *BPdatabase.py* module, loads the configuration and the W90 files and two parameters: the material name and the 2DES confinement direction (as *hkl* indices). The *BPdatabase.py* module contains the information arising from DFT calculations, like the lattice parameter, the lowest unoccupied level (LUL) and the number of MLWFs in the basis among others. In the current version of *BinPo* (v1.1) allowed materials are those with cubic and hexagonal unit-cell and arbitrary Wannierized band manifolds. The 2DES must be confined along [001] direction, but for cubic unit-cells it is possible to access to [110] and [111] confinement directions by using a rotation algorithm described in Appendix H. In the especial case of cubic ABO_3 perovskites only considering the t_{2g} manifold, additional post-processing features explained in Section 4.3 are implemented. After a successful pre-processing, the slab Hamiltonian for a specific material along certain direction will appear in the *BinPo* folder under the name $Hr + material + hkl$.

The next step is to perform the SC potential calculation, as indicated by the workflow in Fig. 4(b). By running the *BP-scp.py* component, the following steps will carry on: necessary modules (numpy, matplotlib, BPmodule, ASE, etc.) are loaded, the parameters are set from the configuration files and/or the command-line,

Table 1
BinPo capabilities: components and their functions.

Component	Description
Pre-processing and SC potential energy calculation	
BP-preproc.py	Pre-processing component. It generates the $Hr + material + hkl$ folder to be loaded in the SC potential calculation and post-processing routines. It runs by command-line without an associated configuration file.
BP-scp.py	Main component. It performs the SC potential energy calculation. Config. file: ∼/*config_files/ scp.yaml*.
Post-processing	
BP-fast_plot.py	Quick plotter tool for the output of *BP-scp.py*. It runs by command-line without an associated configuration file.
BP-bands.py	Band structure component. It performs a band structure calculation, which can include orbital character or bands projections onto planes. Config. file: ∼/*config_files/bands.yaml*.
BP-energy_slices.py	Energy slices component. It performs the calculation of any energy slice (*e.g.* Fermi surface). Config file: ∼/*config_files/energy_slices.yaml*.
BP-energy_plot.py	Plotter component for *BP-energy_slices.py* output. Config. file: ∼/*config_files/energy_plot.yaml*.
BP-orb_density.py	Component to decompose the electron density according to the orbital character. Config. file: ∼/*config_files/orb_density.yaml*. At the moment, available only for cubic ABO_3 with t_{2g} manifold systems.
BP-envelope_wfs.py	Component to compute the envelope wavefunctions at the Γ-point. Config. file: ∼/*config_files/envelope_wfs.yaml*. At the moment, available only for cubic ABO_3 with t_{2g} manifold systems.

the files in $Hr + material + hkl$ folder are loaded and calculation is done. Every file (including a *.log* file) is saved to a new folder with an exclusive name, the identifier, defined by the user for every calculation. Each post-processing step after this point will call the files inside the output folder of the SC potential calculation without modifying its content, except for the *.log* file. For instance, the band structure with *BP_bands.py* or the Fermi surface with *BP_energy-slices.py* can be computed and the outputs will be saved to the respective identifier folder. The details about the use of *BinPo* can be found in *README.md* file within the *BinPo* folder and in ∼/*BPexamples*. The capabilities of *BinPo* through the different components are summarized in Table 1. Each component has an associated configuration file (except for *BP-preproc.py* and *BP-fast_plot.py*) for reading default values of the parameters in case the user does not provide them by command-line.

In Fig. 4(b) can be seen that *BinPo* calls a calculation module named *BPmodule.py*. This is the main module holding the classes and methods. In Section 2.2 the concepts of the slab Hamiltonian and the potential energy along the slab were introduced. These quantities find their counterparts with the Quasi2DHamiltonian *class* and the PotentialEnergy *class* inside this module. These classes contain the fundamental methods to execute the Schrödinger-Poisson scheme. There is a third class called CrystalFeatures, which addresses the crystallography issues of the system. In the next section we will show a complete example of how to use *BinPo* from command-line to compute several quantities of a 2DES formed at STO(001).

4. Examples

In this section, we will show an entire calculation example with *BinPo* for the archetypal STO(001) 2DES. However, the same steps could be followed to compute the physical quantities for different allowed systems. Importantly, we have aimed to organize the input method in a modular manner, so that the user can enter parameter values by command-line, whereas the omitted values are read from the specific configuration files (see Table 1). Moreover, the configuration files are carefully structured to be easily customizable. The description for each parameter of the configuration files can be read from ∼/*config_files*/*help_config.md*. To obtain from command-line a list of parameters that can be modified, the user should type:

$ python BP-component.py -h

being *BP-component.py* any of the components of *BinPo*. By doing so, a list of the basic updatable parameters will appear. The configuration file settings along with the command-line typing for all the examples presented in this section can be found in ∼/*BPexamples*.

4.1. Pre-processing step

Firstly, the user must perform the pre-processing step by typing in the command-line:

$ python BP-preproc.py -mt STO -cfd 001

Note that the material and the 2DES confinement direction, must be indicated by means of *mt* and c*fd* parameters, respectively. After finishing the pre-processing for a specific material/direction combination, the $Hr + material + hkl$ folder will appear. It is important to note that this component should be run only once per material/direction combination. For cubic systems the allowed confinement directions are [001], [110] and [111], whereas for the hexagonal ones only the [001] direction is allowed. Subsequent SC potential calculations and post-processing steps will call the files from $Hr + material + hkl$ folder.

Before we step into the SC potential energy calculation and output post-processing, we must point out that the Fermi level is set to zero and is defined as the LUL (taken from the *BPdatabase.py* module) plus a shift-from-LUL parameter (present in the *scp.yaml* configuration file and updatable by command-line). Consequently, all the energies in the calculations are referred to the Fermi level.

4.2. Self-consistent potential energy calculation

Once the slab Hamiltonian is stored, calculations of the electrostatic properties, such as the SC potential energy, electron density, electric field, etc. can be obtained after specifying the slab size, boundary conditions and k-point grid sampling among other quantities. To achieve this, the user should run the SC potential energy calculation component as:

$ python BP-scp.py -id run1 -mt STO -cfd 001 -tl 40 -nk 26 -bc1 -0.22

In the above command-line we first indicate to *BinPo* that the identifier (*id*) is "run1". It will remain exclusive for this calculation and can be recalled in post-processing steps. The material (*mt*) is STO and the slab consists of 40 planes (*tl*) stacked along the (001) direction (*cfd*) and computed in a k-grid (*nk*) of 26 × 26 points. The boundary condition at the top-most layer (*bc1*) is −0.22 eV.

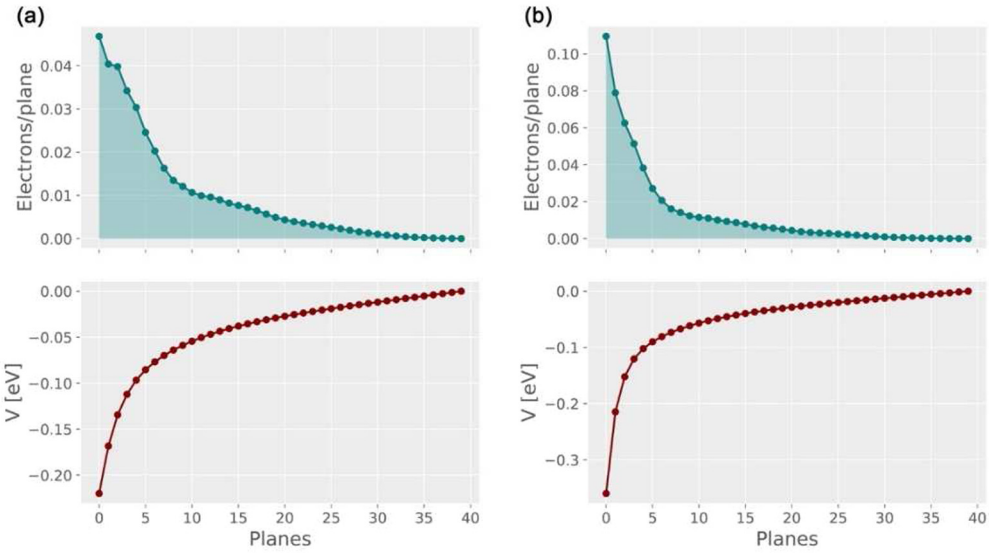

Fig. 5. SC solutions of STO(001) 2DES (top: electron density, bottom: SC potential) with (a) bc1 = −0.22 eV and (b) bc1 = −0.36 eV boundary conditions at the top-most layer.

Note that this boundary condition defines the amount of charge in the system. The outputs of this calculation will be saved to *run1* folder. At the end of the calculation, the user will find a *.dat* file holding the SC solution, the. *log* and the. *yaml* configuration file with the parameters involved. In general, convergence testing for some of the parameters is desirable. An example of convergence analysis for the k-grid that supports the values used here is shown in Appendix G.

After the calculation is done, the user may try to vary the boundary condition value at the top-most layer, for example −0.36 eV, but this time the identifier (*id*) must be updated:

$ python BP-scp.py -id run2 -mt STO -cfd 001 -tl 40 -nk 26 -bc1 -0.36

Note that we modify uniquely the parameters that we need to update, while the other ones remain the same. Now the user will find another folder with the identifier *run2* inside the *BinPo* one. Both the potential energy and the electron density as a function of planes, plotted with *BP-fast_plot.py* tool, are shown in Fig. 5.

4.3. Post-processing steps

Once the user has done the SC potential energy calculation, each post-processing component can be executed independently. In this section we will show how to run such components.

4.3.1. Band structure calculations

The *BP-bands.py* component can compute the band structure in several ways. The first one is what we call "total band structure", which corresponds to the electronic bands without including any projection. On the other hand, two different projections, onto orbitals or planes, can be computed as we will see below.

Total band structure

To compute the total band structure the user can type for example:

$ python BP-bands.py -id run2 -ph XGX -kp 600 -tk 0 -nb 50

Here, the path in the irreducible BZ1 between high symmetry points (*ph*) is specified to be X-Γ-X and it contains 600 points in k-space (*kp*). The path in the *x*-axis will be always expressed in $Å^{-1}$ in the outputs. The energy scale in *y*-axis is expressed in eV and defined respect to the Fermi level. The task parameter (*tk*) equal to 0 indicates that band structure is calculated without projections and the number of bands (*nb*) to calculate will be 50. The user could also select a different path, for example:

$ python BP-bands.py -id run2 -ph MGM -kp 600 -tk 0 -nb 50

Both output plots are shown in Fig. 6(a) and (b).

BinPo also allows for simulating specific regions of interest in the band structure. For example, in order to closely examine the unconventional Rashba spin-splitting, which emerges near the avoided crossings, the user could type:

$ python BP-bands.py -id run2 -ph GX -kp 600 -tk 0 -nb 50 -xy 0.06 0.28 -0.15 -0.015

In this case, a shorter path *ph* was selected (Γ-X), but the number of k-points was kept constant, thus a higher resolution zoomed image is obtained. Additionally, the *xy* parameter was introduced, which stablishes the *x* and *y* limit values of the energy-momentum plot window. The output of this calculation is shown in Fig. 6(c).

So far, we have not considered the possible influence of additional manifolds like the O 2*p*. The Fig. 7 shows how the band structure remains almost the same under the inclusion of the O 2*p* orbitals. In fact, the energy differences for the three first light subbands are less than 2.5 meV, which is a value far below of the typical experimental resolutions. In addition, the computational cost to get the SC potential energy and post-process the output is strongly increased, *e.g.* including the 18 O 2*p* MLWFs, it becomes more than 30x slower. Taking both aspects: band energy differences and computational costs into account, it is reasonable to consider only the t_{2g} manifold in the present case. Although the incorporation of a lower energy manifold does not produce significant changes in the outputs for this STO example, the situation could be different for other materials. Testing band energy differences and computational costs, with the inclusion of more elements in the MLWFs basis, is highly recommended as a first step when the electronic properties of a new material are computed.

Further comparisons tests of the bulk band structure can be taken between the Wannierization and the DFT bands, as included in Appendix A.

Band structure with orbital character

The results of the total band structure can be projected onto the contribution of each orbital, referred as orbital projection. At present, this option is only available for cubic systems with t_{2g} manifold, like the STO and KTO 2DES. The user can obtain it in the current calculation by typing the following:

$ python BP-bands.py -id run2 -ph MGX -kp 1000 -tk 1 -nb 50 -xy -0.25 0.5 -0.35 0.03

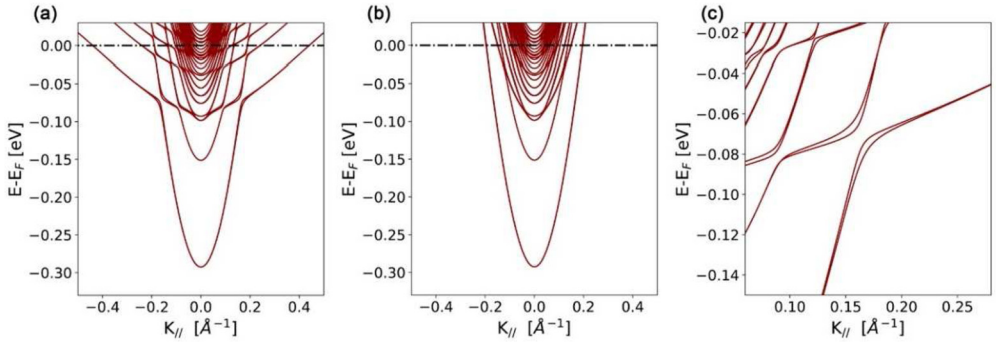

Fig. 6. Output plots of total band structure calculation for STO(001) 2DES along (a) the X-Γ-X and (b) the M-Γ-M high symmetry paths in the irreducible BZ1. (c) Close view of the avoided crossing region where the unconventional Rashba spin-splitting is observed.

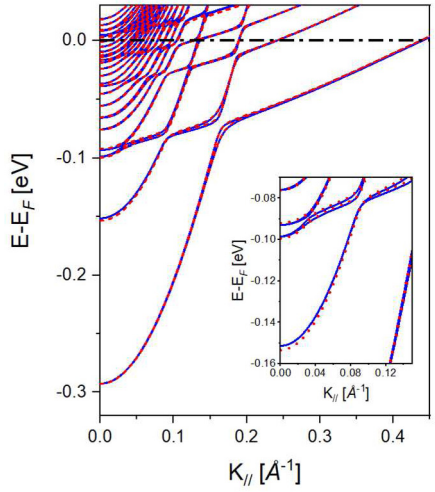

Fig. 7. Comparison of total band structure calculation for STO(001) 2DES along Γ-X high symmetry path considering only the t_{2g} manifold (continue blue line) and considering the t_{2g} plus the O $2p$ manifolds (dashed red line). Insert: close up view to the second light band region.

Now we have selected the M-Γ-X path and *tk* equal to 1 means that the band structure is projected onto the different orbitals in the t_{2g} manifold. The relative weight of the orbitals (d_{xy}, d_{yz}, d_{zx}) is represented by a RGB color code (the user can change the color trio in the *bands.yaml* configuration file). We chose to use a finer discretization along the path with *kp* equal to 1000. The resulting output can be seen in Fig. 8(a). To get a close-up view in the avoided crossing region, the user can type:

$ python BP-bands.py -id run2 -ph GX -kp 1200 -tk 1 -nb 50 -xy 0.06 0.27 -0.15 -0.015

Note that now we just specify the G-X path. Additionally, the discretization along the path was increased with *kp* equal to 1200 and the list of values of the *xy* parameter is enclosing the region of interest. The resulting output can be seen in Fig. 8(c).

Band structure projected onto planes

We can calculate the contribution of a set of planes to the total band structure, referred as plane projection. The user can compute such a projection by typing:

$ python BP-bands.py -id run2 -ph MGX -kp 1000 -tk 2 -nb 50 -xy -0.25 0.5 -0.35 0.03 -pi 0 -pf 2

This line indicates the plane projection task by setting *tk* equal to 2. The planes for projections are established by means of the initial plane (*pi*) and final plane (*pf*) parameters, and the set will range from *pi* to *pf*-1. The above example will project the total band structure onto the first two planes. The output is shown in Fig. 8(b).

4.3.2. Energy slices

As another part of post-processing, we can compute the set of k-points whose eigenenergies are at a specific energy cut, which is named energy slice. For each k-point, there will be $N_\alpha \times L$ eigenenergies, but only if values within a small energy window below the energy cut are found, the k-point, eigenenergies and eigenstates will be considered. This filtering applied on a dense k-grid allows generating high quality slices without the need for interpolation of the points. This component can be run by typing:

$ python BP-energy_slices.py -id run2 -ec 0.0 -nk 300 -ba 60 -bf 0.7

The energy cut (*ec*), in eV, in which the slice will be taken is set to 0.0. Then, we construct a denser k-grid (*nk*) of 300 × 300 points sampling the BZ1, which will be split in 60 batches (*ba*). The reason for defining batches is the reduction of the Hamiltonian size, in this case to (300 × 300)/60 Hamiltonian matrices, with the subsequent reduction of memory consumption, resulting in the need for less resources and computation time. The k-box factor parameter (*bf*) is to enlarge or reduce the BZ1. Note that by setting $ec = 0.0$ we are computing the Fermi surface. The x and y axes of the output energy slices will be always expressed in Å^{-1}. For comparing the results, we can also calculate an energy slice for a different energy cut, for instance, 50 meV below the Fermi level:

$ python BP-energy_slices.py -id run2 -ec -0.05 -nk 300 -ba 60 -bf 0.7

Due to the significant computational cost of using a coarse grid, once this component finishes an output file is automatically saved to the identifier folder, then we must apply the *BP-energy_plot.py* component to plot the results. The plots for these two examples are shown in Fig. 9(a) and (b).

It is possible to compute the energy slices for specific regions of the BZ1. In this way, the resolution can be increased at the same computational cost. For example, the unconventional Rashba spin-splitting can be now closely examined by typing:

$ python BP-energy_slices.py -id run2 -ec 0.0 -nk 300 -ba 60 -bf 0.06 -dk 0.09 -0.17

Note that the k-grid extension is reduced by setting *bf* equal to 0.06. In addition, we are using the k-grid offset parameter (*dk*), which is chosen to be near the area of interest. The output plot associated to this energy slice calculation is shown in Fig. 7(c).

4.3.3. Other capabilities

At present, the additional capabilities that we will exemplify in this section are available for cubic ABO_3 with t_{2g} manifold systems. For the sake of completeness, we show here how to compute the orbital decomposition of the electron density and the envelope wavefunctions of the system. The first quantity allows for analyzing the contribution of the different orbitals to the total electron density. It can be computed by using the *BP-orb_density.py* component as:

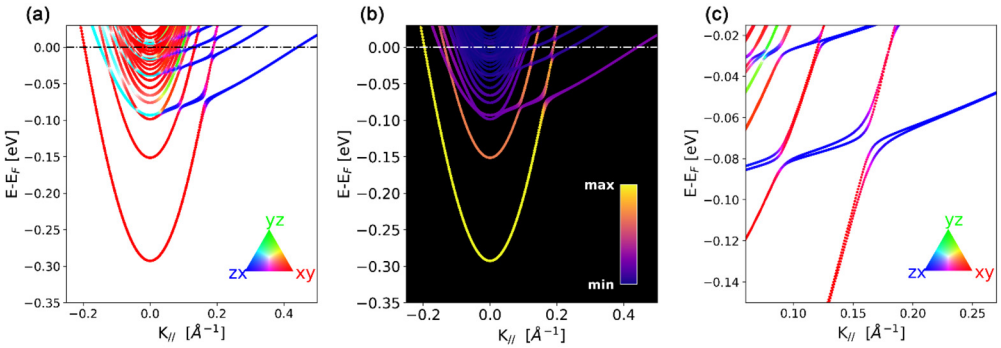

Fig. 8. Band structure for STO(001) 2DES (a) Orbitally projected and (b) projected onto the first two planes along the high symmetry M-Γ-X path. (c) Close-up view of the Rashba spin-splitting with orbital projections.

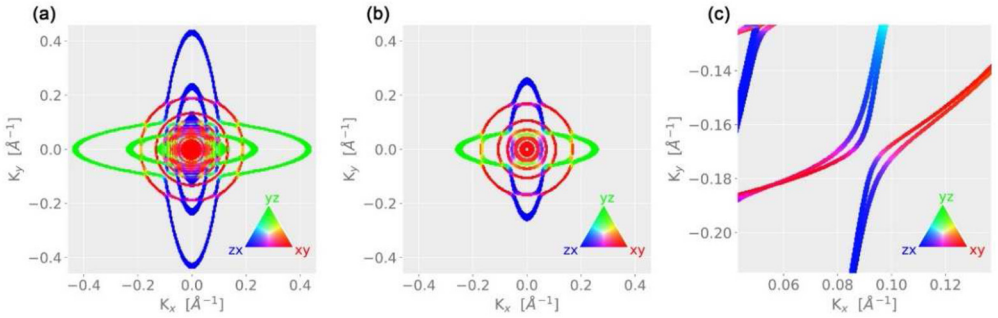

Fig. 9. Energy slices plot for STO(001) 2DES at (a) $ec = 0.0$ (Fermi surface) and (b) $ec = -0.05$ eV. (c) Close-up view to the avoided crossing region where unconventional Rashba spin-splitting is observed.

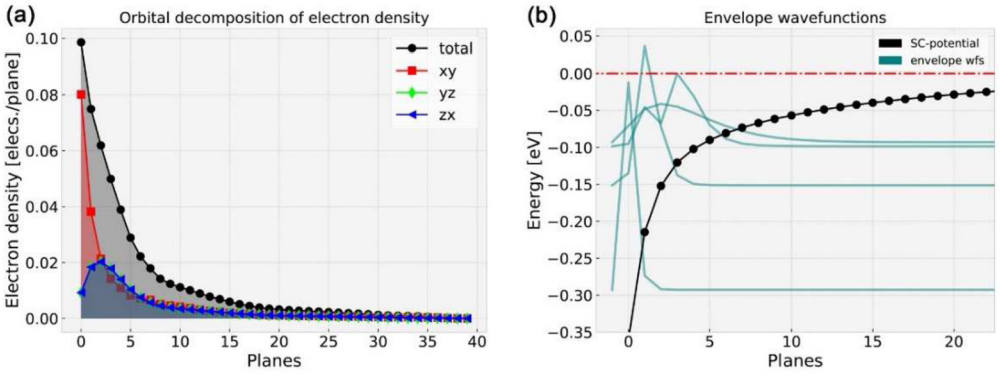

Fig. 10. Further post-processing steps in STO(001) 2DES: (a) orbital decomposition of electron density and (b) the first four pairs of envelope wavefunctions.

$ python BP-orb_density.py -id run2 -aa 0.3

where, we set the curves opacity (*aa*) to 0.3. The output is shown in Fig. 10(a), where the total and partial electron densities are indicated accordingly.

Now we want to compute the envelope wavefunctions at the Γ-point. These $r_\perp$-dependent wavefunctions reflect the quantum confinement near the surface or interface. It can be computed by using the *BP-envelope_wfs.py* component and typing:

$ python BP-envelope_wfs.py -id run2 -sf 0.3 -nw 8 -xy -2 22.5 -0.35 0.06

here we specify the scale factor (*sf*), which affects the amplitude of the envelope wavefunctions, the number of these wavefunctions (*nw*) to compute and the *x* and *y* limits of the plot by means of the *xy* parameter. The output is shown in Fig. 10(b), where the first four pairs of envelope wavefunctions are shown.

4.4. Comparison with experiments

4.4.1. Stabilized 2DES on the bare (001) surface of STO

Several groups have studied experimentally the electronic band structure of the 2DES created at the bare surface of different oxides or at the LAO/STO interface. Here we focus on ARPES [67,68] experiments, since it allows for a direct comparison of the results obtained in *BinPo*. The band structure of the 2DES will have a strong influence in the transport properties of the system and thus, comparisons with experimental results of quantum oscillations [69] and spin transport [34] are possible but require additional modeling and assumptions. In Fig. 11(a) and 11(d) we show ARPES measurements of the electronic band dispersion and the Fermi surface for the 2DES stabilized on the (001) bare surface of STO [8,25,70]. A full description of the measurement conditions can be found in [8]. The energy-momentum dispersions on Fig. 11(a) consist of a ladder of at least three light bands, usually called subbands, which are a clear signature of quantum confinement near the surface. Additionally, we observe a single heavy band of only

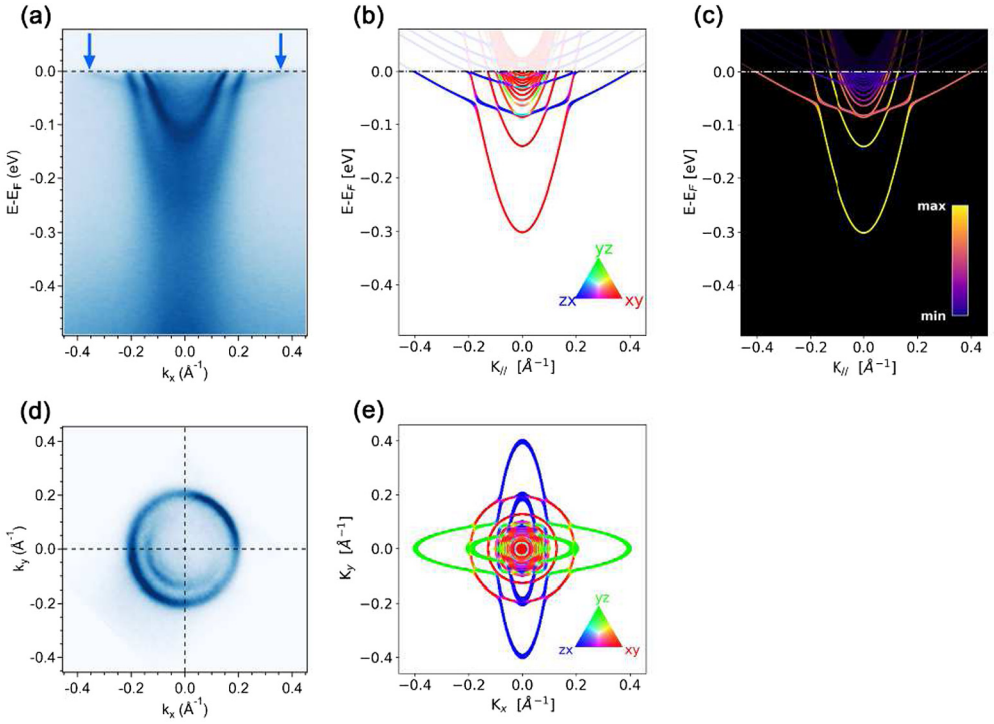

Fig. 11. ARPES measurement of the 2DES stabilized at the bare STO(001) and *BinPo* simulations. (a) Bands dispersions measured along X-Γ-X path (the blue arrows indicate the Fermi momentum for the heavy bands). Band structure calculation with orbital projections (b) and projected onto the first 4 planes (c). (d) Fermi surface. (e) *BinPo* simulation of the Fermi surface with orbital projections.

∼50 meV bandwidth in contrast with the ∼300 meV in the case of the first light sub-band indicating a strong breaking of the t_{2g} orbital degeneracy present in bulk STO. The observed light and heavy sub-bands contribute with circular and elliptical Fermi surface sheets respectively as observed in Fig. 11(d), in the present case the heavy state appears with very low intensity as a consequence of the geometry of the experiment.

In Fig. 11(b) and 11(e) we show calculations performed with *BinPo* of the band structure along the X-Γ-X high symmetry path and the Fermi surface, respectively. In the calculation the potential energy at the surface top-most layer is a free parameter and determines the bandwidth and total charge in the system. In the present case, it was chosen so that the total bandwidth of the first light sub-band coincides with the experimental value of ∼300 meV. Calculations for different band-widths and densities can be found elsewhere [71]. There is a good overall agreement with the experimental data for both the electronic band dispersion and the Fermi surface. The relative sub-band energy and Fermi wave vector for these three light bands is well described by the model. In Fig. 11(c) we show the band-structure projected onto the first 4 planes, the bands that appear with maximum intensity in this figure will be also more intense in the measured ARPES spectra due to the surface sensitivity of the technique. A similar argument and the unfavorably experimental geometry explain why the heavy bands appear faint in the Fermi surface measurements shown in Fig. 11(d). However, taking advantage of polarized light it was shown that multiple heavy sub-bands are present in the 2DES as shown in the *BinPo* calculation [72]. We notice that, while the effective mass of the light sub-bands is well described by the model, there is a clear discrepancy with that of the heavy bands, whose mass renormalization due to electron-phonon and electron-electron interactions is not considered in *BinPo*, a detailed discussion for these effects on STO can be found in Ref. [25].

Using polarized synchrotron light, it can be experimentally demonstrated that the light and heavy bands have predominant d_{xy} and $d_{zx/yz}$ orbital character, respectively [9,25,72]. This observation is in agreement with the calculated orbital character shown in Fig. 11(b) where the light bands appear mostly red corresponding to d_{xy} orbitals and the heavy bands appear blue or green depending on whether the orbital character is d_{zx} or d_{yz}. Interestingly, at the crossing points of the heavy and light bands the orbital character is mixed and the unconventional Rashba spin-splitting is maximized [25,34]. While *BinPo* gives a clear picture of the spin-splitting in these so-called avoided crossings, there are contradicting ARPES experimental reports regarding these details of the electronic structure [27,73]. Evidence from spin-transport experiments support the band structure presented here indicating that *BinPo* is a useful tool to calculate the spin texture of 2DESs with relevance in spintronics [34].

4.4.2. Giant Rashba-type spin-splitting in the bismuth tellurohalide BiTeBr

As an example of application of *BinPo* on systems with hexagonal symmetry, where the electron confinement is produced along the *c* axis, we chose BiTeBr. This compound is part of the so-called bismuth tellurohalides (BiTeX) polar semiconductors, which present a striking bulk Rashba-like effect that leads to novel features. A 2DES emerges at the surface of *n*-doped BiTeX with a high potential to apply such systems in spintronic devices [35–37,74].

In Fig. 12(a) we show the total bandstructure computed along the K-Γ-K path. The details for the *BinPo* calculations can be read in the ∼/*BPexamples* folder. Interestingly, in the present case a ladder of strong Rashba-split sub-bands pairs is observed in our *BinPo* based calculations. The calculated Fermi surface is shown in Fig. 12(c) where the large Rashba-splitting in the compound results in the characteristic Fermi contours. In Fig. 12(b) we show the band structure calculation projected onto the first four layers of the material. This result indicates that in a surface sensitive ARPES experiment the first two pairs of sub-bands should appear with similar intensity whereas the third pair will appear fainter. Indeed, measurements of the electronic structure of BiTeBr can be found in Ref. [37] and the agreement between our calculations and the

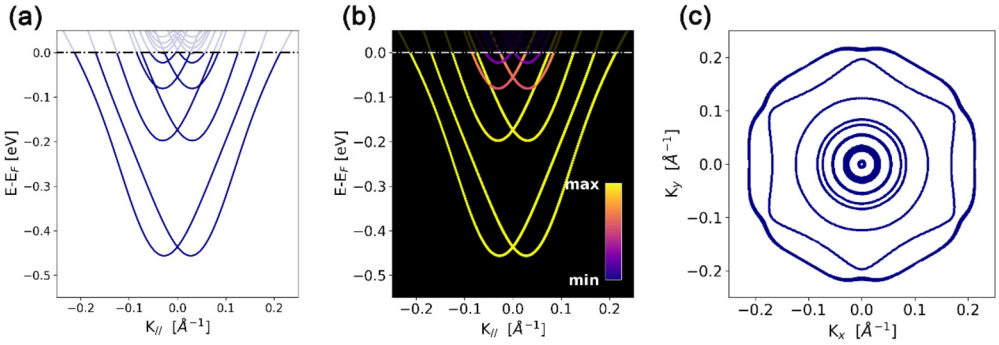

Fig. 12. *BinPo* calculations for BiTeBr: (a) Total band structure computed along the K-Γ-K high symmetry path. (b) Band structure projected onto the first four layers. (c) BiTeBr Fermi surface in the BZ1, where K_x (K_y) corresponds to the K-Γ-K (M-Γ-M) path.

ARPES spectra is good, this highlights the fact that starting from relativistic calculations is useful to reproduce the spin texture of confined 2DES using *BinPo*.

5. Summary and conclusions

We have introduced *BinPo*, an open-source code to compute the band structure and other electronic properties of the 2DES generated at the surface or interface of a variety of cubic and hexagonal crystallographic systems. The code has additional features for the relevant case of cubic ABO_3 perovskites where the t_{2g} manifold plays a central role, like the quantum paraelectrics STO and KTO. The code is written in Python 3.x, so it can run in all platforms in a computationally efficient manner. The files required by *BinPo* are based on first-principles calculations followed by the ML-WFs obtention with the open-source Wannier90 program. We have provided some Wannier90 files to work with, but the user can append others. We have shown how *BinPo* solves the Schrödinger-Poisson scheme to get the SC potential energy, and then calculate post-processing quantities like the band structure, energy slices and envelope wavefunctions among others. The validity of the results, which were all obtained in a conventional laptop computer, is illustrated by direct comparison with ARPES experiments. The ease-of-use of *BinPo* sets the stage for an extended adoption, by scientists looking for a fast and reliable description of the 2DES band structure, helping to understand the experimental results in these novel materials.

Declaration of competing interest

The authors declare that they have no known competing financial interests or personal relationships that could have appeared to influence the work reported in this paper.

Data availability

Data will be made available on request.

Acknowledgements

This work has been supported by Comunidad de Madrid, Spain (Atracción de Talento grant No. 2018-T1/IND-10521) and by MICINN, Spain PID2019-105238GA-I00. Financial support from the Spanish MICINN PID2021-122980OB-C51 and Santander-UCM project PR87/19 is acknowledged (JIB). We acknowledge Alejandro B. Kolton for fruitful discussions and Felix Baumberger for sharing raw ARPES data used to produce Figs. 11(a) and 11(d).

Table A.1
Details of final spread and its components (in Å^2) obtained after the Wannierization of the STO t_{2g} manifold.

Final spread			
Total, Ω	Gauge-invariant, Ω_I	Off-diagonal, Ω_{OD}	Diagonal, Ω_D
11.4649	11.4493	0.0155	0.0000

Appendix A. Details of DFT calculation and wannierization for STO. Available W90 files in *BinPo*

DFT details

The DFT calculations were performed using the open-source Quantum Espresso program [46]. We used the projector augmented wave (PAW) method [75] and the standard PBE exchange-correlation (XC) functional [76]. The PAW PBE full-relativistic pseudopotentials required to describe core electrons were taken from PSlibrary [77]. The non-core electronic configuration encompassed the Ti: $3s, 4s, 3p, 3d$, the O: $2s, 2p$ and the Sr: $4s, 5s, 4p, 5p$ orbitals. The Brillouin zone was sampled with a $15 \times 15 \times 15$ k-mesh Monkhorst-Pack grid method [78]. The cutoff energy for the plane-waves was 70 Ry, whereas for the electron density it was 600 Ry. The convergence threshold for self-consistent field (SCF) calculations was set to 10^{-10} Ry. The electron smearing was selected as fixed because of the insulating nature of the material. After performing SCF unit cells calculations and fitting to Murnaghan equation of state [79] we obtained the lattice parameter values $a_{STO} = 3.9425$ Å.

Wannierization details

The Wannierization and the calculation of the real space Hamiltonian were done using the open-source Wannier90 software [43–45]. Due to fact that the t_{2g} manifold is an isolated groups of bands, a disentanglement was not needed [80]. The KS states were projected onto the t_{2g} manifold within the cubic unit-cell, which encompasses the Ti $3d_{zx}$, $3d_{yz}$, $3d_{xy}$ orbitals. We used 200 iterations in the minimization procedure to ensure convergence. The difference between consecutive total spreads of Wannier functions was less than 10^{-11} Å^2. The individual final spreads were of 1.9108 Å^2 with all the Wannier centers located at the Ti positions, with an uncertainty of less than 10^{-7} Å. In Table A.1, we summarize the total final spread and its components. In Fig. A.1 we show a comparison between the DFT band structure and the Wannierized t_{2g} manifold for STO. We found that the energy differences are below 10^{-3} eV.

List of available W90 files in *BinPo*

We have included in ∼/*WFolder* some W90 files to use in *BinPo*. All available files are listed below in Table A.2. Additional information can be seen in the *BPdtabase.py* module. For those readers interested in adding new W90 files, a detailed and stepwise guide can be found in ∼/*BPexamples* folder.

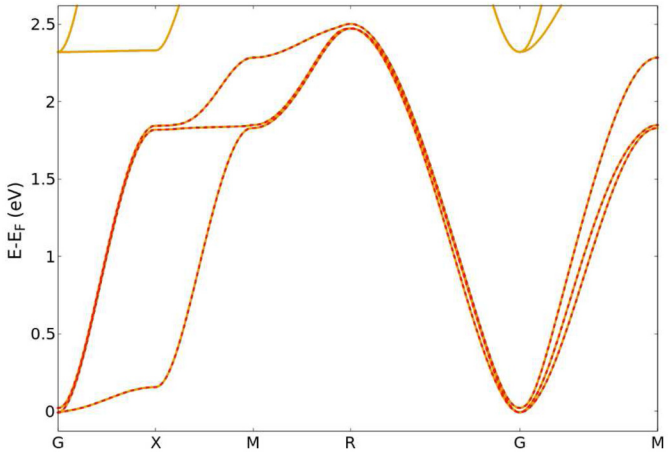

Fig. A.1. Comparison of the STO band structure obtained by DFT calculations (solid orange) versus the Wannierized Ti t_{2g} band manifold (dashed red).

Table A.2
W90 files included with *BinPo*.

System	Filename
STO, Ti t_{2g}	*STO_hr.dat*
STO, Ti $t_{2g} + O2p$	*STOB_hr.dat*
STO, Ti $t_{2g} + e_g$	*STOC_hr.dat*
KTO, Ta t_{2g}	*KTO_hr.dat*
BiTeBr	*BTB_hr.dat*

Appendix B. Post-processing calculations

The eigenstates of Eq. (11) contain useful information of the system through the coefficients $u^{\mathbf{k}_\parallel n}_{\alpha r_\perp}$. So that, once the SC potential is found, other properties can be computed. In particular, we will define two projection operators to get information about the orbital character in the band structure or energy slices, as well as the contribution of different planes to the band structure. In the following, the orthogonality properties of the MLWFs basis of Eq. (4) are used to compute the expectation values.

Orbital projection

At present, this operation is only available for cubic ABO_3 systems with t_{2g} manifold. Recalling the orbital index α from Eq. (7), which spans the t_{2g} manifold, we can define the orbital projector onto the orbital α as:

$$\hat{P}_\alpha = \sum_{r_\perp} \left| \mathbf{R}_\parallel \alpha r_\perp \right\rangle \left\langle \mathbf{R}_\parallel \alpha r_\perp \right| \tag{B.1}$$

The expectation value of this operator for a given eigenstate, namely, the α-orbital character is:

$$C^{\mathbf{k}_\parallel n}_\alpha \equiv \left\langle \phi_{\mathbf{k}_\parallel n} \mid \hat{P}_\alpha \mid \phi_{\mathbf{k}_\parallel n} \right\rangle = \sum_{r_\perp} \left(u^{\mathbf{k}_\parallel n}_{\alpha r_\perp} \right)^* u^{\mathbf{k}_\parallel n}_{\alpha r_\perp} \tag{B.2}$$

Projections onto planes

We will now define the single plane projector, analogously to Eq. (B.1), as:

$$\hat{\Pi}_{r_\perp} = \sum_{\alpha} \left| \mathbf{R}_\parallel \alpha r_\perp \right\rangle \left\langle \mathbf{R}_\parallel \alpha r_\perp \right| \tag{B.3}$$

Note that in this case the expectation value of $\hat{\Pi}_{r_\perp}$ comprises the contribution of the plane at $r_\perp$ to the total band structure. We may be interested in analyzing the contribution of a consecutive set of planes rather than the contribution of a single plane. Therefore, we define the plane projector of a set as $\hat{P}_{r'_\perp, r''_\perp} = \sum_{r_\perp} \hat{\Pi}_{r_\perp}$ with $r_\perp$ in the interval $\left[r'_\perp, r''_\perp - 1\right] \subseteq [0,\ L-1]$. The expectation value for a given eigenstate is:

$$C^{\mathbf{k}_\parallel n}_{r'_\perp, r''_\perp} \equiv \left\langle \phi_{\mathbf{k}_\parallel n} \mid \hat{P}_{r'_\perp, r''_\perp} \mid \phi_{\mathbf{k}_\parallel n} \right\rangle = \sum_{r_\perp = r'_\perp}^{r''_\perp} \sum_{\alpha} \left(u^{\mathbf{k}_\parallel n}_{\alpha r_\perp} \right)^* \left(u^{\mathbf{k}_\parallel n}_{\alpha r_\perp} \right) \tag{B.4}$$

Orbital decomposition of electron density

At present, this operation is only available for cubic ABO_3 systems with t_{2g} manifold. It is useful to find out the partial contribution of the orbitals to the charge density ($\rho(r_\perp)$) along the slab. By retaining the index α from Eq. (13) it is possible to get such a quantity $\rho_\alpha(r_\perp)$ defined by:

$$\rho_\alpha(r_\perp) = -\frac{|e|}{\Omega_\perp N_\parallel} \sum_{\mathbf{k}_\parallel n} f\left(\epsilon_{\mathbf{k}_\parallel n}, T\right) \left| u^{\mathbf{k}_\parallel n}_{\alpha r_\perp} \right|^2 \tag{B.5}$$

Envelope wavefunctions at the Γ-point

At present, this operation is only available for cubic ABO_3 systems with t_{2g} manifold. It is useful to visualize the potential-well diagram associated to the SC potential confining the charge. We will be particularly interested at the Γ-point, where the bandwidth is maximum. There, the so-called envelope wavefunctions are defined as:

$$\xi^\alpha_{\mathbf{\Gamma} n}(r_\perp) = \sum_\alpha \left(u^{\mathbf{\Gamma} n}_{\alpha r_\perp} \right)^* u^{\mathbf{\Gamma} n}_{\alpha r_\perp} \tag{B.6}$$

Note that, despite their different dependences, this equation is similar to Eq. (B.2). In fact, Eq. (B.6) can be easily inferred using a proper projection operator like Eqs. (B.1) and (B.3).

Appendix C. Fixed background density approach

The presence of in-gap states in STO was reported in several works [81–83]. These states are generally associated to defects. When the charge is transferred to the interface and the 2DES emerges, some electrons could be trapped in these localized states [84,85]. For this reason, we include a minimal approach in *BinPo* to consider such states, whose trapped charge could influence the band structure as well. We follow the approach implemented in other works [86–88]. We rewrite Eq. (15) with a slight modification:

$$\frac{d^2 V(r_\perp)}{dr_\perp^2} = \frac{|e|}{\varepsilon_0 \varepsilon_r [E(r_\perp)]} \left(\rho(r_\perp) + \rho_{def}(r_\perp) \right) \tag{C.1}$$

where $\rho_{def}(r_\perp)$ is the profile of fixed charge along the slab, which is an unknown quantity. This simple approach consists of treating this charge distribution as $\rho_{def}(r_\perp) = \rho_d \Theta(L_d - r_\perp)$, with ρ_d the constant charge per plane, L_d the extension of this charge (from the top-most layers toward the bulk) and Θ the Heaviside step function.

The choice to set the background electron occupation can be accessed in the configuration file for the SC potential energy calculation, *~/config_files/scp.yaml*. In Fig. C.1 we show how the band structure is modified when a constant charge of 0.01 electrons per plane along the whole slab is considered. For the calculation shown in Fig. C.1(b), the integrated free charge and fixed charge are approximately the same. The user can reproduce both calculations of Fig. C.1 by looking at *~/BPexamples*. Notice that the in-gap states are not included in the band structures shown in Fig. C.1. The mobile charge in Fig. C.1(b) is less than in Fig. C.1(a), as a result of the interaction to the fixed background charge modeling the presence of the in-gap states.

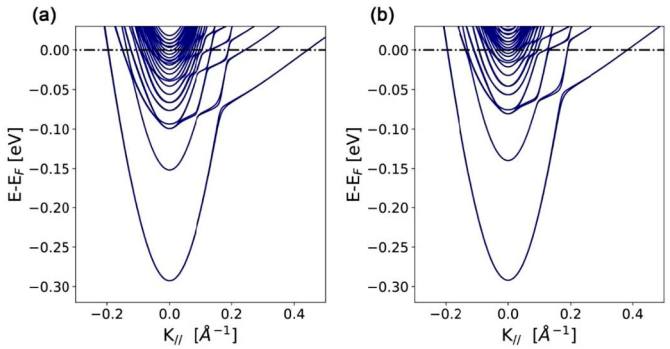

Fig. C.1. Modification on the band structure induced by a fixed charge background to simulate defects. (a) STO(001) 2DES total band structure along M-Γ-X path. (b) Same as (a) including an additional charge of 0.01 electrons per plane.

Appendix D. Deduction of the charge density equation. Validity of orthogonality relations in the slab

In order to obtain the expression for the charge density, it would be instructive to start from the bulk case. Consider the bulk Hamiltonian matrix $H^{(\mathbf{k})}$ whose elements are given by Eq. (2). Then, the bulk eigenenergies $\varepsilon_{\mathbf{k}n}$, with the associate eigenstates $|\phi_{\mathbf{k}n}\rangle$, can be straightforwardly obtained by diagonalization. In turn, these eigenstates, considering the Eq. (1), can be expanded in term of $|\mathcal{W}_{\mathbf{k}\alpha}\rangle$ states [39] as:

$$|\phi_{\mathbf{k}n}\rangle = \sum_{\alpha} u_{\alpha}^{\mathbf{k}n} |\mathcal{W}_{\mathbf{k}\alpha}\rangle \tag{D.1}$$

where α spans a specific manifold (see Eqs. (6) and (7) in Section 2.2) and the resulting normalization condition reads $\sum_{\alpha} \left|u_{\alpha}^{\mathbf{k}n}\right|^2 = 1$. We can compute the 3D electron density, $\rho_b(\mathbf{r})$, directly from the eigenstates as:

$$\rho_b(\mathbf{r}) = -|e| \sum_{\mathbf{k}n} f(\varepsilon_{\mathbf{k}n}, T) \left|\langle \mathbf{r} \mid \phi_{\mathbf{k}n}\rangle\right|^2 \tag{D.2}$$

Now, we calculate the mean electron density in the bulk by averaging over all space. By the orthogonalization properties of the MLWFs basis, we find:

$$\begin{aligned} \overline{\rho}_b &= \frac{1}{N\Omega} \int_{\Omega} d\mathbf{r} \rho_b(\mathbf{r}) = -\frac{|e|}{N\Omega} \sum_{\mathbf{k}n} f(\varepsilon_{\mathbf{k}n}, T) \sum_{\alpha} \left|u_{\alpha}^{\mathbf{k}n}\right|^2 \\ &= -\frac{|e|}{N\Omega} \sum_{occup.} 1 \end{aligned} \tag{D.3}$$

where $\Omega = a^3$ is the volume of the cubic cell, with a being the lattice parameter and N is the number of k-points in the first Brillouin zone (BZ1). It has to be noticed that the last term in Eq. (D.3) contains the total number of occupied states, so that it returns an intuitive result.

Following the same arguments, we could try to compute the electron density for the slab system and the corresponding average bulk density. In analogy with Eq. (D.2) we could write:

$$\rho_s(\mathbf{r}) = -|e| \sum_{\mathbf{k}_{\parallel}n} f\left(\varepsilon_{\mathbf{k}_{\parallel}n}, T\right) \left|\left\langle \mathbf{r} \mid \phi_{\mathbf{k}_{\parallel}n}\right\rangle\right|^2 \tag{D.4}$$

$$\overline{\rho}_s = \frac{1}{N_{\parallel}\Omega_{\perp}} \int_{\Omega_{\perp}} d\mathbf{r} \rho_s(\mathbf{r}) = -\frac{|e|}{N_{\parallel}\Omega_{\perp}} \sum_{\mathbf{k}_{\parallel}n} f\left(\varepsilon_{\mathbf{k}_{\parallel}n}, T\right) \sum_{\alpha, r_{\perp}} \left|u_{\alpha r_{\perp}}^{\mathbf{k}_{\parallel}n}\right|^2 \tag{D.5}$$

where $\Omega_{\perp}$ is the interplanar volume as defined in Eq. (14) of Section 2.3.2 and $N_{\parallel}$ the number of $\mathbf{k}_{\parallel}$-points in the 2D BZ1. Note that the last sum could be replaced by 1 according to the eigenstates normalization. Nevertheless, we want to define a plane dependent electron density. By retaining the $r_{\perp}$ index in the last term, the electron density can be defined as:

$$\rho(r_{\perp}) \equiv \overline{\rho}_s^{(r_{\perp})} = -\frac{|e|}{N_{\parallel}\Omega_{\perp}} \sum_{\mathbf{k}_{\parallel}n} f\left(\varepsilon_{\mathbf{k}_{\parallel}n}, T\right) \sum_{\alpha} \left|u_{\alpha r_{\perp}}^{\mathbf{k}_{\parallel}n}\right|^2 \tag{D.6}$$

that is finally the Eq. (13) shown in Section 2.3.2.

Regarding the validity of orthogonality relations in the Eqs. (4), it is worth noting that these relations will be exact if the slab is created by replicating the unit-cell along a lattice vector ($\mathbf{R}$) direction. This is because the interplanar and the bulk unit-cell volume is the same, $\Omega_{\perp} = \Omega$, and the Wannier functions are periodic in $\mathbf{R}$ by definition. A different situation takes place if a r-space rotation is applied on the slab. The Eqs. (4) will be no longer exact, given that either the volume or shape of the rotated unit-cell is different than the original ones. Therefore, these relations become:

$$\begin{aligned} \left\langle \mathbf{R}'_{\parallel} \alpha' r'_{\perp} \mid \mathbf{R}_{\parallel} \alpha r_{\perp} \right\rangle &\cong \delta_{\mathbf{R}_{\parallel}\mathbf{R}'_{\parallel}} \delta_{\alpha\alpha'} \delta_{r_{\perp} r'_{\perp}} \\ \left\langle \mathcal{W}_{\mathbf{k}_{\parallel}\alpha' r'_{\perp}} \mid \mathcal{W}_{\mathbf{k}_{\parallel}\alpha r_{\perp}} \right\rangle &\cong \delta_{\mathbf{k}_{\parallel}\mathbf{k}'_{\parallel}} \delta_{\alpha\alpha'} \delta_{r_{\perp} r'_{\perp}} \end{aligned} \tag{D.7}$$

Nevertheless, the Eqs. (D.7) will be still a good approximation since the MLWFs have a strong localization, which is a main requisite in any tight-binding approach. This localization is quantified by means of the spread functional [39]. The smaller this spread the stronger the localization. The validity of the relations (D.7) is fundamental to compute the charge density from Eq. (D.6) under the plane-by-plane discretization approach given by the interplanar volume, $\Omega_{\perp}$. The criterion that we have considered here is the following: if the square root of the largest individual spread, *i.e.* the largest spread among all the MLWFs, is below the lattice parameters values, we take the Eqs. (D.7) as valid. For example, in Appendix A we have shown that the individual spread for each of the MLWFs in the STO was 1.9108 Å^2, while the optimized lattice parameter turned out to be 3.9425 Å and hence the criterion is satisfied.

Appendix E. 1D Poisson equation

Deduction of the non-linear Poisson equation

In non-linear media, the relation between the electric field E and the electric displacement D is $dD = \varepsilon_0 \varepsilon_r(E) dE$, where $\varepsilon_r(E)$ is the field dependent relative permittivity, whose nature is differential. An interesting discussion about the physical meaning of the implied quantities can be found elsewhere [89].

In order to obtain the Poisson equation, we should introduce an expression for D in the Gauss law, $\frac{dD}{dr_{\perp}} = \rho$, but the differential relation $dD = \varepsilon_0 \varepsilon_r(E) dE$ must be linearized. We can define the average relative permittivity as:

$$\overline{\varepsilon}(E) \equiv \frac{1}{E} \int_{E} \varepsilon_r\left(E'\right) dE' \tag{E.1}$$

By definition, $\overline{\varepsilon}(E)$ satisfies the linear relation $D = \varepsilon_0 \overline{\varepsilon}(E) E$, in consequence, we can now replace D in the Gauss law:

$$\begin{aligned} \frac{dD}{dr_{\perp}} &= \frac{d}{dr_{\perp}} \left(\varepsilon_0 \overline{\varepsilon}(E) E\right) = \frac{d}{dr_{\perp}} \left(\varepsilon_0 \int_{E} \varepsilon_r\left(E'\right) dE'\right) \\ &= \varepsilon_0 \varepsilon_r(E) \frac{dE}{dr_{\perp}} = \rho \end{aligned} \tag{E.2}$$

Using the relation between the electric field and the potential energy, $E(r_{\perp}) = \frac{1}{|e|} \frac{dV(r_{\perp})}{dr_{\perp}}$, we finally obtain the Poisson equation:

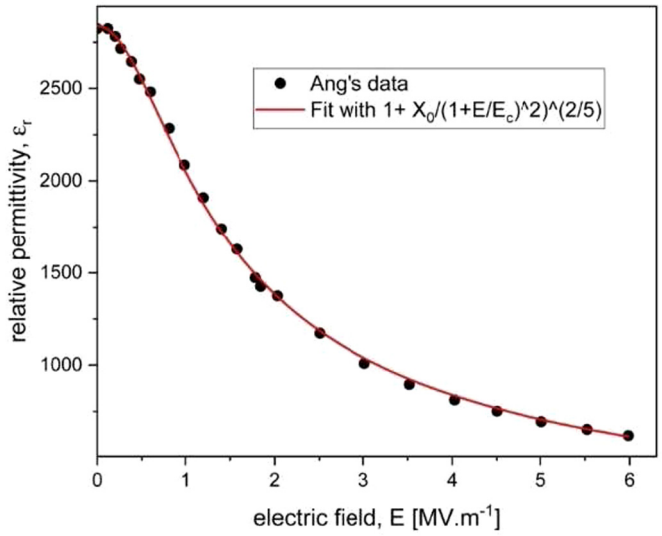

Fig. E.1. Fit of the experimental Ang's data using a sigmoid-like function. The values obtained from the fitting are $\chi_0 = 2837$ and $E_c = 892244\ \mathrm{V\,m^{-1}}$.

$$\frac{d^2V(r_\perp)}{dr_\perp^2} = \frac{|e|}{\varepsilon_0 \varepsilon_r[E(r_\perp)]}\rho(r_\perp) \tag{E.3}$$

Comments on relative permittivity models

It is worth noting that a crucial element in Eq. (E.3) is the electric field-dependent relative permittivity, $\varepsilon_r[E]$. Indeed, this introduces the non-linearity in the Poisson equation, and such expressions are of the uttermost importance for solving it. When ε_r is constant, like in most of the semiconductors, the Eq. (E.3) is linear. On the other hand, for materials like the quantum paraelectrics, ε_r is strongly dependent on E and it has a profound impact on the potential energy profile. So that we need to know this dependency. We could get the functional form of $\varepsilon_r[E]$ from theoretical considerations or from phenomenological fittings of experimental and theoretical data. For STO(001), Copie et al. [90] have derived an expression at low temperatures, which is used in *BinPo* as a pre-defined model. In Fig. E.1, we show an example of how to obtain a permittivity model by fitting the Ang's experimental data [52] with a sigmoid-like function. This is the pre-defined model for KTO(001) in *BinPo*. There are a few works in the literature that could be useful to either use or determine these empirical models (see Refs. [22,53–55,91–94]).

We take the functional form of the relative permittivity derived from experimental data as a good starting point. However, an accurate description of relative permittivity as a function of the electric field, and even as a function of the defect density, is a rather intricate problem which is out of the scope of this work. This is the main reason whereby *BinPo* has the feature of working with any functional form as input.

Comments on boundary conditions

Since the Poisson equation (Eq. (E.3)) is a second order differential equation, we must explicit two boundary conditions. *BinPo* allows for using Dirichlet boundary conditions at top- and bottom-most layers, *i.e.*, to set the values $V(0)$ (surface) and $V(L-1)$ (bulk). It is also available to use the mixing Dirichlet-Neumann boundary conditions, namely, to set the values $V(0)$ and $\frac{d}{dr_\perp}V(L-1) = 0$. The latter one is especially useful in two situations: (a) if it is desired to truly know the value of convergence for $V(r_\perp)$ when $r_\perp \to \infty$ (very large L), or (b) if it is observed that under the present conditions the potential is confined enough to quickly overcome some $V(L-1)$ used as Dirichlet boundary condition. This last case will produce a non-physical behavior of the potential energy profile along the slab. Information about the implementation of the boundary conditions can be read in the next Appendix.

Appendix F. Solving the non-linear 1D Poisson equation by finite differences method

The finite differences method (FDM) [95] is, along with finite elements, one of the most popular numerical methods to solve differential equations. We have implemented an iterative solver for Poisson equation in *BinPo*. The derivatives of the unknown function, $V(r_\perp)$ in this case, are approximated as finite differences. Let ℓ label the planes perpendicular to the (hkl) confinement direction, the first and second derivatives of $V(r_\perp)$ under this approximation read:

$$\frac{dV(r_\perp)}{dr_\perp} \approx \frac{1}{\Delta r_\perp}\left(V_{\ell+\frac{1}{2}} - V_{\ell-\frac{1}{2}}\right) \tag{F.1}$$

$$\frac{d^2V(r_\perp)}{dr_\perp^2} \approx \frac{1}{\Delta r_\perp^2}\left(V_{\ell+1} + V_{\ell-1} - 2V_\ell\right) \tag{F.2}$$

where ℓ spans the discrete integer list $[0, L-1]$, being L the number of planes in the slab. In Eq. (F.1) the values $V_{\ell\pm\frac{1}{2}}$ are found by linear interpolation. Note that due to the discretization applied to this problem, $\Delta r_\perp$ is the interplanar distance, whose product with the area $\|\overline{a}_1 \times \overline{a}_2\|$, gives the interplanar volume $\Omega_\perp$ (see Eq. (14) in Section 2.3.2). We will take advantage of the expression of the relative permittivity in terms of electric field, E, which in turn is proportional to the first derivative of $V(r_\perp)$. Replacing the derivatives, the approximate Poisson equation reads:

$$\frac{1}{\Delta r_\perp^2}\left(V_{\ell+1} + V_{\ell-1} - 2V_\ell\right) \approx \frac{|e|}{\varepsilon_0 \varepsilon_r[E_\ell]}\rho_\ell \tag{F.3}$$

with $E_\ell = \frac{1}{|e|\Delta r_\perp}\left(V_{\ell+\frac{1}{2}} - V_{\ell-\frac{1}{2}}\right)$.

Note that we use the notation $\varepsilon_r[E_\ell]$ to emphasize that the relative permittivity is a functional of the electric field E_ℓ. Generally, for any initial guess of $V(r_\perp)$, Eq. (F.3) will not be satisfied. Thus, an equality in this equation must be enforced. If we reorder the terms and introduce the iteration index j, it is possible to express the ℓ-th element of the potential energy for the $(j+1)$-th iteration as:

$$V_\ell^{j+1} = \frac{1}{2}\left(V_{\ell+1}^j + V_{\ell-1}^j - \frac{\Delta r_\perp^2 |e| \rho_\ell}{\varepsilon_0 \varepsilon_r[E_\ell]}\right) \tag{F.4}$$

By many iterations over all ℓ's (except for the boundaries, whose values are determined by the boundary conditions), the numerical solution of Poisson equation can be found.

As mentioned above, the iteration procedure in Eq. (F.4) does not need to consider the potential at the boundaries, so that now ℓ spans the reduced integer list $[1, L-2]$. In the case of Dirichlet's boundary conditions, $V_0 = bc1$ and $V_{L-1} = bc2$ are set, where *bc1* and *bc2* are input values. For mixing Dirichlet-Neumann boundary conditions instead, $V_0 = bc1$ and $V_{L-1} = V_{L-2}$ are used, where the second condition is obtained straightforwardly by the simple backward difference expression of $\frac{d}{dr_\perp}V(L-1) = 0$ in FDM. The error between the j-th and $(j+1)$-th potentials is evaluated according to:

$$\chi_P^2 = \frac{1}{L}\sum_{l=0}^{L-1}\left(\frac{V_\ell^{j+1} - V_\ell^j}{V_0}\right)^2 \tag{F.5}$$

Finally, the solution is found where χ_P^2 is less than a convergence threshold. In our case we set the condition $\chi_P^2 < 3 \times 10^{-12}$.

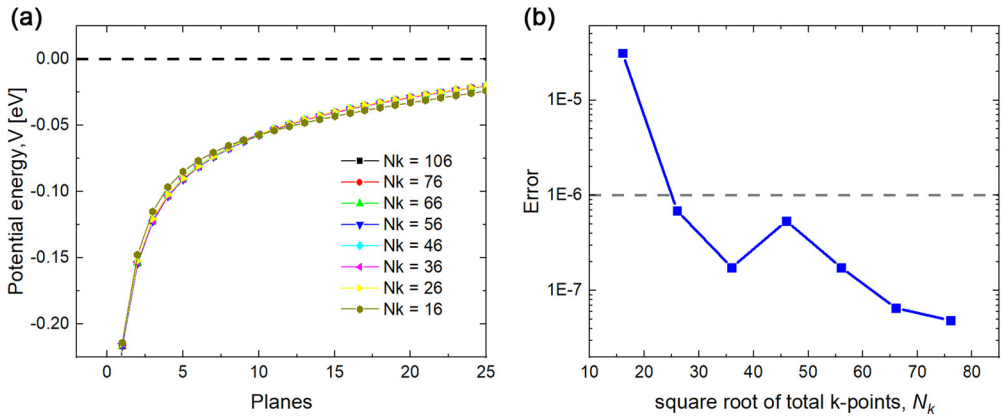

Fig. G.1. (a) SC solutions for different values of N_k (here $L = 40$ but the SC potentials were plotted up to 25 planes). (b) Error computed among the SC potential and the reference (SC potential with $N_k = 106$).

We did not demonstrate theoretically the convergence of this method, but we observed a well convergent behavior for multiple cases with the predefined relative permittivity models, as well as many others that were introduced as input in *BinPo*.

Appendix G. Convergence analysis

K-grid convergence analysis

In *BinPo*, for a given material (W90 file) and a confinement direction, the SC solution is determined by the value and type of the boundary conditions, number of planes, convergence threshold for potential, relative permittivity model and, of course, the k-grid sampling. We want to show the convergence analysis for one of the most relevant parameters: the number of points in the k-grid sampling ($N_k \times N_k$). Actually, we will talk about N_k, which is the input parameter. We will also assume that the k-grid offset was already settled. Ideally, $N_k \to \infty$ is desired because it will give the best quantitative result that the code can provide within the approximations considered. However, in order to reduce the computational cost, we need to limit the N_k value, increasing the result uncertainty. This is a rather common problem in numerical simulations, and a criterion must be taken to decide when the solution is accurate enough. For example, if we take $N_k = 106$ as reference of well-converged SC potential, we can compute the error between this potential and the other SC potentials (Fig. G.1(a) displays all the SC potentials) by means of Eq. (16) in Section 2.3.4. We look for the minimal value of N_k that produces an error less than the convergence threshold, which from the Fig. G.1(b) is ${N_k}^{conv} = 26$. For a fast calculation, the user could set values for $N_k < {N_k}^{conv}$. However, if an accurate SC solution is desirable, the user should set $Nk \geq {N_k}^{conv}$. Ultimately, we want to remark that the same analysis could be done for the number of planes and with difference convergence thresholds if a clear criterion is set. The criteria could be imposed also over the electron density if this quantity is of major interest. The details for all these calculations can be found in ∼/*BPexamples*.

Number of planes to be considered

Another important quantity to be tested is the number of planes, L, used in the simulations. Ideally, a very large L along with Neumann boundary condition at bottom-most layer (*bc2*) is desirable for the 2DES formed at the surface or interface of a semi-infinite system. However, the larger the system the more computationally expensive the calculation. It is then useful, from a practical point of view, to perform calculations with a reduced number of planes. We then need to compare the latter SC potential with that obtained for large L values. The comparison should be made in the region of interest of our physical problem defined by the first L_{cut} planes. A satisfactory comparison takes place when both SC potentials do not differ appreciably in the region of interest and, hence, the band structures are almost indistinguishable. In the following, we exemplify the procedure for a particular case.

In order to stablish a criterion in the case of a 2DES on the (100) surface of STO, we compare here different SC potentials obtained with either Neumann (N) or Dirichlet (D) and different L's, named as $V^L(r_\perp)$'s. Firstly, we performed a realistic calculation to get a reference SC potential, $V^{ref}(r_\perp)$, using $L = 200$ and *bc2* $= N$. We then considered an L_{cut} value of 15 planes to compute the error between the different $V^L(r_\perp)$'s and $V^{ref}(r_\perp)$. We chose this L_{cut} since the electron number per plane amounts to 10% of the profile maximum. The criterion could be different depending on how strong the confinement in the particular system is. In Fig. G.2(a), we show the comparison between different $V^L(r_\perp)$'s and the $V^{ref}(r_\perp)$. It is worth observing that the larger the L the more similar the potentials to the reference one, no matter the *bc2* chosen. We use equation (G.1) to estimate the error, χ^2_{Lcut}, within the interval $[0, L_{cut} - 1]$.

$$\chi^2_{Lcut} = \frac{1}{L_{cut}} \sum_{r_\perp=0}^{L_{cut}-1} \left(\frac{V^L(r_\perp) - V^{ref}(r_\perp)}{V^L(r_\perp = 0)} \right)^2 \tag{G.1}$$

The dimensionless χ^2_{Lcut} values as function of L are shown in Fig. G.2(b). It can be seen that the *bc2* $= D$ is a better approximation up to the crossover at $\sim$ 65 planes. However, the χ^2_{Lcut} is less than 10^{-4} from $L = 40$ and *bc2* $= D$. Therefore, we consider this L value as appropriate to describe the 2DES under study in this example.

We strongly recommend the users to perform a calculation for a large enough L in order to check that the SC potential corresponds to what is expected in a real physical situation.

Appendix H. Change of basis + rotation algorithm for other crystal faces in cubic crystallographic systems

The 3D bulk TB Hamiltonian actually holds all the information needed to inspect other crystal faces defined by a generic $\vec{v} =$ [*hkl*] normal direction. We introduce here the simple algorithm to create slabs and compute quantities along other crystallographic directions. It consists of two steps: (i) change of basis from the original cartesian to the new one, (ii) rotation of the new $\vec{v}$ vector into the [001] direction.

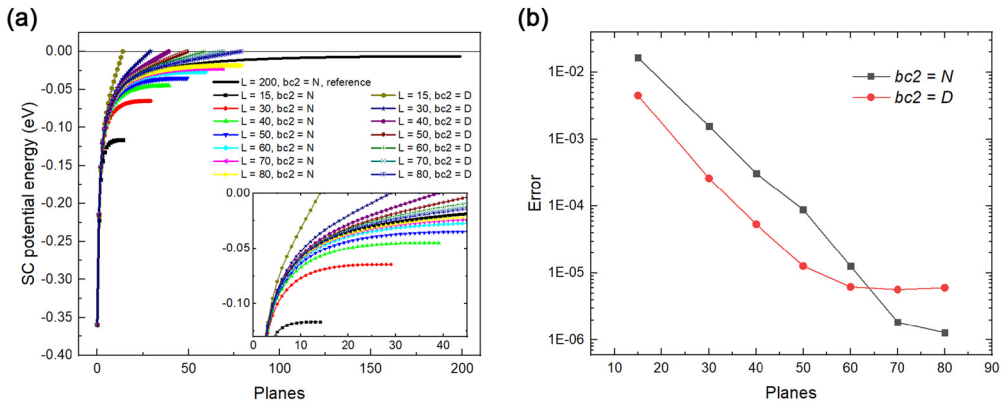

Fig. G.2. (a) SC potentials for different values of L and $bc2$ = Neumann (N) and Dirichlet (D). Insert: a close-up view to the region of interest. (b) Error computed among the SC potentials and the reference using $_{Lcut} = 15$ in Eq. (G.1).

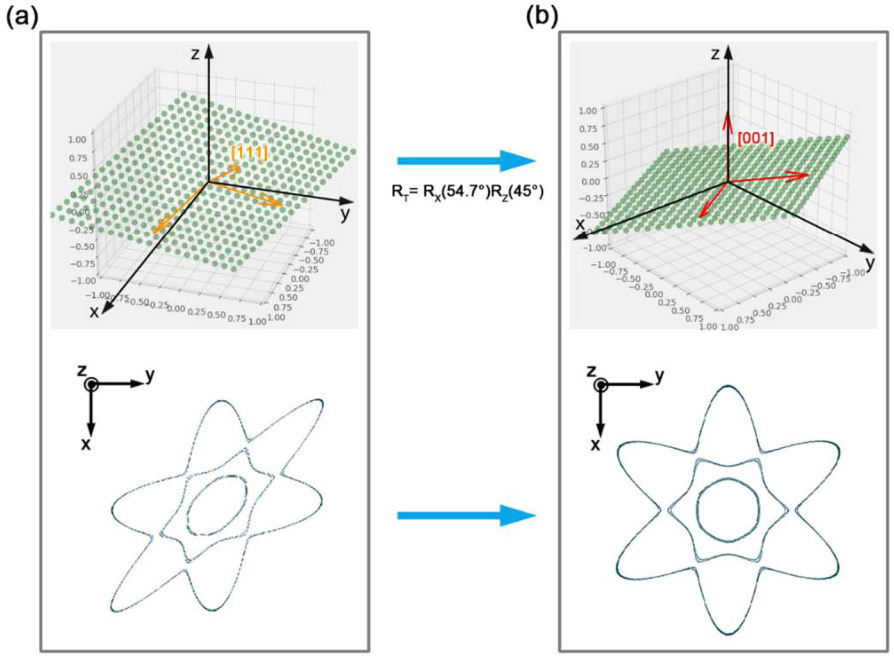

Fig. H.1. Illustration of the method to compute the energy slices along other confinement directions: (a) once the change of basis was applied to compute the slice and (b) after applying the 3D rotation that solves the distortions.

(i) Change of basis

It is proper to write explicitly the exponential factor of the 2D Fourier transform in Eq. (3) of the main text, which contains the crystallographic information. First of all, the actual expression used inside the code must be pointed out:

$$e^{i\mathbf{k}_\parallel\cdot\mathbf{R}_\parallel} \rightarrow e^{i2\pi\mathbf{k}_\parallel\cdot\mathbf{R}_\parallel} \tag{H.1}$$

with real and reciprocal vectors given by:

$$\mathbf{R}_\parallel = r_1\mathbf{a_1} + r_2\mathbf{a_2}, \mathbf{k}_\parallel = k_1\mathbf{b_1} + k_2\mathbf{b_2} \quad \text{and} \quad \mathbf{a}_i\cdot\mathbf{b}_j = \delta_{ij} \tag{H.2}$$

with r_i, k_j real coefficients. Note that for $\vec{v} = [001]$, the basis $\mathbf{B} = \{\mathbf{a_1}, \mathbf{a_2}\}$ is the defined by {[1,0,0], [0,1,0]}. Consider now $\vec{v}$ in an arbitrary direction, thus, a new basis $\mathbf{B'} = \{\mathbf{a}'_1, \mathbf{a}'_2\}$ for the 2D real space and the associated reciprocal basis $\underline{\mathbf{B}}_\mathbf{k}' = \{\mathbf{b}'_1, \mathbf{b}'_2\}$ must be considered. Now, we can write arbitrary real and reciprocal vectors analogously to Eq. (H.2). Let the new coefficients be $\tilde{r}_i, \tilde{k}_j$, then the exponent in Eq. (H.1) is invariant under changes of basis, as proven below:

$$e^{i2\pi\mathbf{k}'_\parallel\cdot\mathbf{R}'_\parallel} = e^{i2\pi\left(\tilde{k}_1\mathbf{b}'_\mathbf{1}+\tilde{k}_2\mathbf{b}'_\mathbf{2}\right)\cdot\left(\tilde{r}_1\mathbf{a}'_\mathbf{1}+\tilde{r}_2\mathbf{a}'_\mathbf{2}\right)} = e^{i2\pi\left(\tilde{k}_1\cdot\tilde{r}_1+\tilde{k}_2\cdot\tilde{r}_2\right)}$$
$$= e^{i2\pi\mathbf{k}_\parallel\cdot\mathbf{R}_\parallel} \tag{H.3}$$

where the last equality can be written because the arbitrary indices $\tilde{r}_i, \tilde{k}_j$ span the same discretized real and reciprocal spaces.

(ii) Rotation

So far, we have seen that a change of basis does not affect the results when the Fourier transform is performed. However, it should be noticed that the new transfer integrals must be carefully assigned to certain k-grid. To illustrate this point, we show an example computed with the energy slice post-processing tool for STO(111) 2DES as illustrated in Fig. H.1. At the top we represented schematically the k-grid. Once you have computed the energy slice for the [111] direction, one can observe the distorted energy slice resulting from it (bottom side of Fig. H.1(a)). This requires rotating the new normal vector into the [001] direction which then produces the correct assignment of k-space symmetries and values (see Fig. H.1(b)).

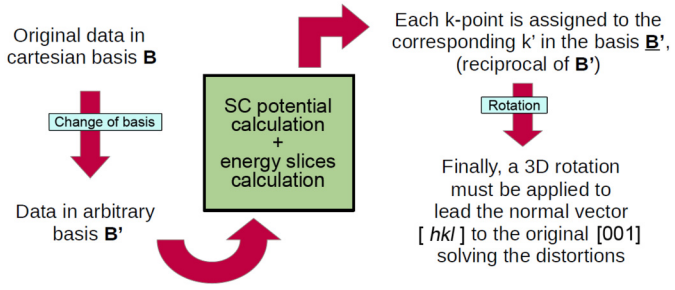

Fig. H.2. Flowchart of the algorithm of change of basis + rotation to analyze other confinement directions.

As a summary, the Fig. H.2 shows the simple flowchart of the complete rotation algorithm.

References

[1] A. Ohtomo, H.Y. Hwang, Nature 427 (2004) 423–426, https://doi.org/10.1038/nature02308.

[2] M. Li, S. Wang, Y. Zhao, K. Jin, Eur. Phys. J. Appl. Phys. 93 (2021) 1–11, https://doi.org/10.1051/epjap/2021200326.

[3] O. Tufte, P. Chapman, Phys. Rev. 155 (1967) 796–802, https://doi.org/10.1103/PhysRev.155.796.

[4] N. Nakagawa, H.Y. Hwang, D.a. Muller, Nat. Mater. 5 (2006) 204–209, https://doi.org/10.1038/nmat1569.

[5] J.N. Eckstein, Nat. Mater. 6 (2007) 473–474, https://doi.org/10.1038/nmat1944.

[6] P.R. Willmott, S.A. Pauli, R. Herger, C.M. Schlepütz, D. Martoccia, B.D. Patterson, B. Delley, R. Clarke, D. Kumah, C. Cionca, Y. Yacoby, Phys. Rev. Lett. 99 (2007) 155502, https://doi.org/10.1103/PhysRevLett.99.155502.

[7] F. Gunkel, C. Bell, H. Inoue, B. Kim, A.G. Swartz, T.A. Merz, Y. Hikita, S. Harashima, H.K. Sato, M. Minohara, S. Hoffmann-Eifert, R. Dittmann, H.Y. Hwang, Phys. Rev. X 6 (2016) 1–15, https://doi.org/10.1103/PhysRevX.6.031035.

[8] S.M. Walker, F.Y. Bruno, Z. Wang, A. de la Torre, S. Riccó, A. Tamai, T.K. Kim, M. Hoesch, M. Shi, M.S. Bahramy, P.D.C. King, F. Baumberger, Adv. Mater. 27 (2015) 3894–3899, https://doi.org/10.1002/adma.201501556.

[9] T.C. Rödel, F. Fortuna, S. Sengupta, E. Frantzeskakis, P. Le Fèvre, F. Bertran, B. Mercey, S. Matzen, G. Agnus, T. Maroutian, P. Lecoeur, A.F. Santander-Syro, Adv. Mater. 28 (2016) 1976–1980, https://doi.org/10.1002/adma.201505021.

[10] S. McKeown Walker, A. de la Torre, F.Y. Bruno, A. Tamai, T.K. Kim, M. Hoesch, M. Shi, M.S. Bahramy, P.D.C. King, F. Baumberger, Phys. Rev. Lett. 113 (2014) 177601, https://doi.org/10.1103/PhysRevLett.113.177601.

[11] L. Dudy, M. Sing, P. Scheiderer, J.D. Denlinger, P. Schütz, J. Gabel, M. Buchwald, C. Schlueter, T.-L. Lee, R. Claessen, Adv. Mater. 28 (2016) 7443–7449, https://doi.org/10.1002/adma.201600046.

[12] M. Gabay, S. Gariglio, J.-M. Triscone, a.F. Santander-Syro, Eur. Phys. J. Spec. Top. 222 (2013) 1177–1183, https://doi.org/10.1140/epjst/e2013-01913-1.

[13] S. Stemmer, S. James Allen, Annu. Rev. Mater. Res. 44 (2014) 151–171, https://doi.org/10.1146/annurev-matsci-070813-113552.

[14] J.I. Beltrán, M.C. Muñoz, Phys. Rev. B 95 (2017) 1, https://doi.org/10.1103/PhysRevB.95.245120.

[15] J.C. Li, J.I. Beltrán, M.C. Muñoz, Phys. Rev. B, Condens. Matter Mater. Phys. 87 (2013) 1–5, https://doi.org/10.1103/PhysRevB.87.075411.

[16] K.V. Shanavas, J. Electron Spectrosc. Relat. Phenom. 201 (2015) 121–126, https://doi.org/10.1016/j.elspec.2014.08.005.

[17] K.V. Shanavas, Z.S. Popović, S. Satpathy, Phys. Rev. B, Condens. Matter Mater. Phys. 90 (2014) 1–9, https://doi.org/10.1103/PhysRevB.90.165108.

[18] K. Janicka, J.P. Velev, E.Y. Tsymbal, Phys. Rev. Lett. 102 (2009) 1–4, https://doi.org/10.1103/PhysRevLett.102.106803.

[19] A. Annadi, Q. Zhang, X. Renshaw Wang, N. Tuzla, K. Gopinadhan, W.M. Lü, A. Roy Barman, Z.Q. Liu, A. Srivastava, S. Saha, Y.L. Zhao, S.W. Zeng, S. Dhar, E. Olsson, B. Gu, S. Yunoki, S. Maekawa, H. Hilgenkamp, T. Venkatesan, A. Ariando, Nat. Commun. 4 (2013) 1–7, https://doi.org/10.1038/ncomms2804.

[20] R. Pentcheva, W.E. Pickett, Phys. Rev. B, Condens. Matter Mater. Phys. 74 (2006) 1–7, https://doi.org/10.1103/PhysRevB.74.035112.

[21] H. Chen, A. Kolpak, S. Ismail-Beigi, Phys. Rev. B, Condens. Matter Mater. Phys. 82 (2010) 1–20, https://doi.org/10.1103/PhysRevB.82.085430.

[22] M. Stengel, Phys. Rev. Lett. 106 (2011) 136803, https://doi.org/10.1103/PhysRevLett.106.136803.

[23] N.C. Bristowe, P. Ghosez, P.B. Littlewood, E. Artacho, J. Phys. Condens. Matter 26 (2014), https://doi.org/10.1088/0953-8984/26/14/143201.

[24] A. Paredes, D.N. Olivieri, H. Michinel, Physica D 403 (2020) 132301, https://doi.org/10.1016/j.physd.2019.132301.

[25] P.D.C. King, S.M.K. Walker, A. Tamai, A. De La Torre, T. Eknapakul, P. Buaphet, S.K. Mo, W. Meevasana, M.S. Bahramy, F. Baumberger, Nat. Commun. 5 (2014), https://doi.org/10.1038/ncomms4414.

[26] F.Y. Bruno, S. McKeown Walker, S. Riccò, A. la Torre, Z. Wang, A. Tamai, T.K. Kim, M. Hoesch, M.S. Bahramy, F. Baumberger, Adv. Electron. Mater. 5 (2019) 1800860, https://doi.org/10.1002/aelm.201800860.

[27] S. McKeown Walker, S. Riccò, F.Y. Bruno, A. De La Torre, A. Tamai, E. Golias, A. Varykhalov, D. Marchenko, M. Hoesch, M.S. Bahramy, P.D.C. King, J. Sánchez-Barriga, F. Baumberger, Phys. Rev. B 93 (2016) 1–5, https://doi.org/10.1103/PhysRevB.93.245143.

[28] S. Birner, T. Zibold, T. Andlauer, T. Kubis, M. Sabathil, A. Trellakis, P. Vogl, IEEE Trans. Electron Devices 54 (2007) 2137–2142, https://doi.org/10.1109/TED.2007.902871.

[29] I. Tan, G.L. Snider, L.D. Chang, E.L. Hu, J. Appl. Phys. 68 (1990) 4071–4076, https://doi.org/10.1063/1.346245.

[30] H. Hebal, Z. Koziol, S.B. Lisesivdin, R. Steed, Comput. Mater. Sci. 186 (2021) 110015, https://doi.org/10.1016/j.commatsci.2020.110015.

[31] Y. Tokura, N. Nagaosa, Science 80 (288) (2000) 462–468, https://doi.org/10.1126/science.288.5465.462.

[32] E. Mikheev, I.T. Rosen, D. Goldhaber-Gordon, Sci. Adv. 7 (2021) 1–8, https://doi.org/10.1126/sciadv.abi6520.

[33] C. Liu, X. Yan, D. Jin, Y. Ma, H.W. Hsiao, Y. Lin, T.M. Bretz-Sullivan, X. Zhou, J. Pearson, B. Fisher, J.S. Jiang, W. Han, J.M. Zuo, J. Wen, D.D. Fong, J. Sun, H. Zhou, A. Bhattacharya, Science 80 (371) (2021) 716–721, https://doi.org/10.1126/science.aba5511.

[34] D.C. Vaz, P. Noël, A. Johansson, B. Göbel, F.Y. Bruno, G. Singh, S. McKeown-Walker, F. Trier, L.M. Vicente-Arche, A. Sander, S. Valencia, P. Bruneel, M. Vivek, M. Gabay, N. Bergeal, F. Baumberger, H. Okuno, A. Barthélémy, A. Fert, L. Vila, I. Mertig, J.P. Attané, M. Bibes, Nat. Mater. 18 (2019) 1187–1193, https://doi.org/10.1038/s41563-019-0467-4.

[35] M.S. Bahramy, N. Ogawa, Adv. Mater. 29 (2017), https://doi.org/10.1002/adma.201605911.

[36] K. Ishizaka, M.S. Bahramy, H. Murakawa, M. Sakano, T. Shimojima, T. Sonobe, K. Koizumi, S. Shin, H. Miyahara, A. Kimura, K. Miyamoto, T. Okuda, H. Namatame, M. Taniguchi, R. Arita, N. Nagaosa, K. Kobayashi, Y. Murakami, R. Kumai, Y. Kaneko, Y. Onose, Y. Tokura, Nat. Mater. 10 (2011) 521–526, https://doi.org/10.1038/nmat3051.

[37] M. Sakano, M.S. Bahramy, A. Katayama, T. Shimojima, H. Murakawa, Y. Kaneko, W. Malaeb, S. Shin, K. Ono, H. Kumigashira, R. Arita, N. Nagaosa, H.Y. Hwang, Y. Tokura, K. Ishizaka, Phys. Rev. Lett. 110 (2013) 1–5, https://doi.org/10.1103/PhysRevLett.110.107204.

[38] N. Marzari, I. Souza, D. Vanderbilt, Highlight Mon, PsiK Newsl. 57 (2003) 129–168.

[39] N. Marzari, A.A. Mostofi, J.R. Yates, I. Souza, D. Vanderbilt, Rev. Mod. Phys. 84 (2012) 1419–1475, https://doi.org/10.1103/RevModPhys.84.1419.

[40] M. Willatzen, L.C. Lew Yan Voon, The k p Method: Electronic Properties of Semiconductors, 1st ed., Springer, Berlin, Heidelberg, 2009.

[41] J.C. Slater, G.F. Koster, Phys. Rev. 94 (1954) 1498–1524, https://doi.org/10.1103/PhysRev.94.1498.

[42] Q.S. Wu, S.N. Zhang, H.F. Song, M. Troyer, A.A. Soluyanov, Comput. Phys. Commun. 224 (2018) 405–416, https://doi.org/10.1016/j.cpc.2017.09.033.

[43] A.A. Mostofi, J.R. Yates, Y.S. Lee, I. Souza, D. Vanderbilt, N. Marzari, Comput. Phys. Commun. 178 (2008) 685–699, https://doi.org/10.1016/j.cpc.2007.11.016.

[44] A.A. Mostofi, J.R. Yates, G. Pizzi, Y.S. Lee, I. Souza, D. Vanderbilt, N. Marzari, Comput. Phys. Commun. 185 (2014) 2309–2310, https://doi.org/10.1016/j.cpc.2014.05.003.

[45] G. Pizzi, V. Vitale, R. Arita, S. Blügel, F. Freimuth, G. Géranton, M. Gibertini, D. Gresch, C. Johnson, T. Koretsune, J. Ibañez-Azpiroz, H. Lee, J.M. Lihm, D. Marchand, A. Marrazzo, Y. Mokrousov, J.I. Mustafa, Y. Nohara, Y. Nomura, L. Paulatto, S. Poncé, T. Ponweiser, J. Qiao, F. Thöle, S.S. Tsirkin, M. Wierzbowska, N. Marzari, D. Vanderbilt, I. Souza, A.A. Mostofi, J.R. Yates, J. Phys. Condens. Matter 32 (2020), https://doi.org/10.1088/1361-648X/ab51ff.

[46] P. Giannozzi, S. Baroni, N. Bonini, M. Calandra, R. Car, C. Cavazzoni, D. Ceresoli, G.L. Chiarotti, M. Cococcioni, I. Dabo, A. Dal Corso, S. De Gironcoli, S. Fabris, G. Fratesi, R. Gebauer, U. Gerstmann, C. Gougoussis, A. Kokalj, M. Lazzeri, L. Martin-Samos, N. Marzari, F. Mauri, R. Mazzarello, S. Paolini, A. Pasquarello, L. Paulatto, C. Sbraccia, S. Scandolo, G. Sclauzero, A.P. Seitsonen, A. Smogunov, P. Umari, R.M. Wentzcovitch, J. Phys. Condens. Matter 21 (2009), https://doi.org/10.1088/0953-8984/21/39/395502.

[47] N. Marzari, D. Vanderbilt, AIP Conf. Proc. 146 (2011) 146–155, https://doi.org/10.1063/1.56269.

[48] F. Stern, J. Comput. Phys. 6 (1970) 56–67, https://doi.org/10.1016/0021-9991(70)90004-5.

[49] M.S. Bahramy, P.D.C. King, A. De La Torre, J. Chang, M. Shi, L. Patthey, G. Balakrishnan, P. Hofmann, R. Arita, N. Nagaosa, F. Baumberger, Nat. Commun. 3 (2012) 1–7, https://doi.org/10.1038/ncomms2162.

[50] S. McKeown Walker, Two Dimensional Electron Liquids at Oxide Surfaces Studied by Angle Resolved Photoemission Spectroscopy, Université de Genevè, 2016.

[51] F. El-Mellouhi, E.N. Brothers, M.J. Lucero, I.W. Bulik, G.E. Scuseria, Phys. Rev. B, Condens. Matter Mater. Phys. 87 (2013) 1, https://doi.org/10.1103/PhysRevB.87.035107.

[52] C. Ang, A.S. Bhalla, L.E. Cross, Phys. Rev. B, Condens. Matter Mater. Phys. 64 (2001) 184104, https://doi.org/10.1103/physrevb.64.184104, 1–6.

[53] C. Ang, Z. Yu, Phys. Rev. B, Condens. Matter Mater. Phys. 69 (2004), https://doi.org/10.1103/PhysRevB.69.174109.
[54] J. Hemberger, P. Lunkenheimer, R. Viana, R. Böhmer, A. Loidl, Phys. Rev. B 52 (1995) 13159–13162, https://doi.org/10.1103/PhysRevB.52.13159.
[55] R.C. Neville, B. Hoeneisen, C.A. Mead, J. Appl. Phys. 43 (1972) 2124–2131, https://doi.org/10.1063/1.1661463.
[56] F. Rana, S. Tiwari, D.A. Buchanan, Appl. Phys. Lett. 69 (1996) 1104–1106, https://doi.org/10.1063/1.117072.
[57] T.E. Oliphant, Comput. Sci. Eng. 9 (2007) 10–20, https://doi.org/10.1109/MCSE.2007.58.
[58] S. Van Der Walt, S.C. Colbert, G. Varoquaux, Comput. Sci. Eng. 13 (2011) 22–30, https://doi.org/10.1109/MCSE.2011.37.
[59] P. Virtanen, R. Gommers, T.E. Oliphant, M. Haberland, T. Reddy, D. Cournapeau, E. Burovski, P. Peterson, W. Weckesser, J. Bright, S.J. van der Walt, M. Brett, J. Wilson, K.J. Millman, N. Mayorov, A.R.J. Nelson, E. Jones, R. Kern, E. Larson, C.J. Carey, İ. Polat, Y. Feng, E.W. Moore, J. VanderPlas, D. Laxalde, J. Perktold, R. Cimrman, I. Henriksen, E.A. Quintero, C.R. Harris, A.M. Archibald, A.H. Ribeiro, F. Pedregosa, P. van Mulbregt, A. Vijaykumar, A. Pietro Bardelli, A. Rothberg, A. Hilboll, A. Kloeckner, A. Scopatz, A. Lee, A. Rokem, C.N. Woods, C. Fulton, C. Masson, C. Häggström, C. Fitzgerald, D.A. Nicholson, D.R. Hagen, D.V. Pasechnik, E. Olivetti, E. Martin, E. Wieser, F. Silva, F. Lenders, F. Wilhelm, G. Young, G.A. Price, G.L. Ingold, G.E. Allen, G.R. Lee, H. Audren, I. Probst, J.P. Dietrich, J. Silterra, J.T. Webber, J. Slavič, J. Nothman, J. Buchner, J. Kulick, J.L. Schönberger, J.V. de Miranda Cardoso, J. Reimer, J. Harrington, J.L.C. Rodríguez, J. Nunez-Iglesias, J. Kuczynski, K. Tritz, M. Thoma, M. Newville, M. Kümmerer, M. Bolingbroke, M. Tartre, M. Pak, N.J. Smith, N. Nowaczyk, N. Shebanov, O. Pavlyk, P.A. Brodtkorb, P. Lee, R.T. McGibbon, R. Feldbauer, S. Lewis, S. Tygier, S. Sievert, S. Vigna, S. Peterson, S. More, T. Pudlik, T. Oshima, T.J. Pingel, T.P. Robitaille, T. Spura, T.R. Jones, T. Cera, T. Leslie, T. Zito, T. Krauss, U. Upadhyay, Y.O. Halchenko, Y. Vázquez-Baeza, Nat. Methods 17 (2020) 261–272, https://doi.org/10.1038/s41592-019-0686-2.
[60] J.D. Hunter, Comput. Sci. Eng. 9 (2007) 90–95, https://doi.org/10.1109/MCSE.2007.55.
[61] A. Hjorth Larsen, J. Jørgen Mortensen, J. Blomqvist, I.E. Castelli, R. Christensen, M. Dułak, J. Friis, M.N. Groves, B. Hammer, C. Hargus, E.D. Hermes, P.C. Jennings, P. Bjerre Jensen, J. Kermode, J.R. Kitchin, E. Leonhard Kolsbjerg, J. Kubal, K. Kaasbjerg, S. Lysgaard, J. Bergmann Maronsson, T. Maxson, T. Olsen, L. Pastewka, A. Peterson, C. Rostgaard, J. Schiøtz, O. Schütt, M. Strange, K.S. Thygesen, T. Vegge, L. Vilhelmsen, M. Walter, Z. Zeng, K.W. Jacobsen, J. Phys. Condens. Matter 29 (2017), https://doi.org/10.1088/1361-648X/aa680e.
[62] E. Teller, J. Phys. Chem. 41 (1937) 109–116, https://doi.org/10.1021/j150379a010.
[63] Z. Zhong, A. Tóth, K. Held, Phys. Rev. B, Condens. Matter Mater. Phys. 87 (2013) 1–5, https://doi.org/10.1103/PhysRevB.87.161102.
[64] L.W. Van Heeringen, G.A. De Wijs, A. McCollam, J.C. Maan, A. Fasolino, Phys. Rev. B, Condens. Matter Mater. Phys. 88 (2013) 1, https://doi.org/10.1103/PhysRevB.88.205140.
[65] A.Y. Bychkov, E.I. Rashba, JETP Lett. 39 (1984) 78–81.
[66] G. Bihlmayer, O. Rader, R. Winkler, New J. Phys. 17 (2015), https://doi.org/10.1088/1367-2630/17/5/050202.
[67] S. McKeown Walker, F.Y. Bruno, F. Baumberger, Springer Ser. Mater. Sci. 266 (2018) 55–85, https://doi.org/10.1007/978-3-319-74989-1_4.
[68] V.N. Strocov, C. Cancellieri, A.S. Mishchenko, Springer Ser. Mater. Sci. (2018) 107–151, https://doi.org/10.1007/978-3-319-74989-1_6.
[69] K. Rubi, J. Gosteau, R. Serra, K. Han, S. Zeng, Z. Huang, B. Warot-Fonrose, R. Arras, E. Snoeck Ariando, M. Goiran, W. Escoffier, npj Quantum Mater. 5 (2020), https://doi.org/10.1038/s41535-020-0210-z.
[70] W. Meevasana, P.D.C. King, R.H. He, S.K. Mo, M. Hashimoto, A. Tamai, P. Songsiriritthigul, F. Baumberger, Z.X. Shen, Nat. Mater. 10 (2011) 114–118, https://doi.org/10.1038/nmat2943.
[71] S. McKeown Walker, M. Boselli, E.A. Martínez, S. Gariglio, F.Y. Bruno, F. Baumberger, Adv. Electron. Mater. 2101376 (2022) 1–8, https://doi.org/10.1002/aelm.202101376.
[72] S. Soltani, S. Cho, H. Ryu, G. Han, B. Kim, D. Song, T.K. Kim, M. Hoesch, C. Kim, Phys. Rev. B 95 (2017) 125103, https://doi.org/10.1103/PhysRevB.95.125103.
[73] A.F. Santander-Syro, F. Fortuna, C. Bareille, T.C. Rödel, G. Landolt, N.C. Plumb, J.H. Dil, M. Radović, Nat. Mater. 13 (2014) 1085–1090, https://doi.org/10.1038/nmat4107.
[74] S.V. Eremeev, I.A. Nechaev, Y.M. Koroteev, P.M. Echenique, E.V. Chulkov, Phys. Rev. Lett. 108 (2012) 1–5, https://doi.org/10.1103/PhysRevLett.108.246802.
[75] P.E. Blöchl, Phys. Rev. B 50 (1994) 17953–17979, https://doi.org/10.1103/PhysRevB.50.17953.
[76] J.P. Perdew, K. Burke, M. Ernzerhof, Phys. Rev. Lett. 77 (1996) 3865–3868, https://doi.org/10.1103/PhysRevLett.77.3865.
[77] A. Dal Corso, Comput. Mater. Sci. 95 (2014) 337–350, https://doi.org/10.1016/j.commatsci.2014.07.043.
[78] D. Monkhorst, H.J. Pack, Phys. Rev. B 13 (1976) 5188–5192, https://doi.org/10.1103/PhysRevB.13.5188.
[79] V.G. Tyuterev, N. Vast, Comput. Mater. Sci. 38 (2006) 350–353, https://doi.org/10.1016/j.commatsci.2005.08.012.
[80] N. Marzari, D. Vanderbilt, Phys. Rev. B, Condens. Matter Mater. Phys. 56 (1997) 12847–12865, https://doi.org/10.1103/PhysRevB.56.12847.
[81] D. Kan, T. Terashima, R. Kanda, A. Masuno, K. Tanaka, S. Chu, H. Kan, A. Ishizumi, Y. Kanemitsu, Y. Shimakawa, M. Takano, Nat. Mater. 4 (2005) 816–819, https://doi.org/10.1038/nmat1498.
[82] G. Drera, F. Banfi, F.F. Canova, P. Borghetti, L. Sangaletti, F. Bondino, E. Magnano, J. Huijben, M. Huijben, G. Rijnders, D.H.A. Blank, H. Hilgenkamp, A. Brinkman, Appl. Phys. Lett. 98 (2011) 1–4, https://doi.org/10.1063/1.3549177.
[83] Y. Li, S.N. Phattalung, S. Limpijumnong, J. Kim, J. Yu, Phys. Rev. B, Condens. Matter Mater. Phys. 84 (2011) 1–6, https://doi.org/10.1103/PhysRevB.84.245307.
[84] C. Ricca, I. Timrov, M. Cococcioni, N. Marzari, U. Aschauer, Phys. Rev. Res. 2 (2020) 23313, https://doi.org/10.1103/physrevresearch.2.023313.
[85] J. Souto-Casares, N.A. Spaldin, C. Ederer, Phys. Rev. Res. 3 (2021) 23027, https://doi.org/10.1103/physrevresearch.3.023027.
[86] F. Stern, Phys. Rev. B 5 (1972) 4891–4899, https://doi.org/10.1103/PhysRevB.5.4891.
[87] S. Gariglio, A. Fête, J.M. Triscone, J. Phys. Condens. Matter 27 (2015), https://doi.org/10.1088/0953-8984/27/28/283201.
[88] P. Armagnat, A. Lacerda-Santos, B. Rossignol, C. Groth, X. Waintal, SciPost Phys. 7 (2019), https://doi.org/10.21468/scipostphys.7.3.031.
[89] H. Peelaers, K. Krishnaswamy, L. Gordon, D. Steiauf, A. Sarwe, A. Janotti, C.G. Van De Walle, Appl. Phys. Lett. 107 (2015), https://doi.org/10.1063/1.4935222.
[90] O. Copie, V. Garcia, C. Bödefeld, C. Carrétéro, M. Bibes, G. Herranz, E. Jacquet, J.L. Maurice, B. Vinter, S. Fusil, K. Bouzehouane, H. Jaffrès, A. Barthélémy, Phys. Rev. Lett. 102 (2009) 1–4, https://doi.org/10.1103/PhysRevLett.102.216804.
[91] R.A. Van Der Berg, P.W.M. Blom, J.F.M. Cillessen, R.M. Wolf, Appl. Phys. Lett. 697 (1995) 697, https://doi.org/10.1063/1.114103.
[92] Y. Matsumoto, S. Takata, R. Tanaka, A. Hachiya, J. Appl. Phys. 109 (2011), https://doi.org/10.1063/1.3530612.
[93] M. Minohara, Y. Hikita, C. Bell, H. Inoue, M. Hosoda, H.K. Sato, H. Kumigashira, M. Oshima, E. Ikenaga, H.Y. Hwang, Sci. Rep. 7 (2017) 3–9, https://doi.org/10.1038/s41598-017-09920-9.
[94] S. Moser, V. Jovic, R. Koch, L. Moreschini, J.S. Oh, C. Jozwiak, A. Bostwick, E. Rotenberg, J. Electron Spectrosc. Relat. Phenom. 225 (2018) 16–22, https://doi.org/10.1016/j.elspec.2018.01.008.
[95] S. Hoffman, J.D. Frankel, Numerical Methods for Engineers and Scientists, Second, Taylor & Francis, 2001.